Assessing the Comparative Effects of Storm-relative Helicity Components within Right-moving Supercell Environments

Nicholas A. Goldacker[a] and Matthew D. Parker,[a]

[a] *Department of Marine, Earth, and Atmospheric Sciences, North Carolina State University, Raleigh, North Carolina*

Corresponding author: Nicholas A. Goldacker, nagoldac@ncsu.edu

Early Online Release: This preliminary version has been accepted for publication in *Journal of the Atmospheric Sciences*, may be fully cited, and has been assigned DOI 10.1175/JAS-D-22-0253.1. The final typeset copyedited article will replace the EOR at the above DOI when it is published.

ABSTRACT: Supercell thunderstorms develop low-level rotation via tilting of environmental horizontal vorticity ($\overrightarrow{\omega}_h$) by the updraft. This rotation induces dynamic lifting that can stretch near-surface vertical vorticity into a tornado. Low-level updraft rotation is generally thought to scale with 0–500 m storm-relative helicity (SRH): the combination of storm-relative flow, $\left|\overrightarrow{SRF}\right|$, $\left|\overrightarrow{\omega}_h\right|$, and cos$\phi$ (where ϕ is the angle between $\overrightarrow{SRF}$ and $\overrightarrow{\omega}_h$). It is unclear how much influence each component of SRH has in intensifying the low-level mesocyclone. This study surveys these three components using self-organizing maps (SOMs) to distill 15,906 proximity soundings for observed right-moving supercells. Statistical analyses reveal the component most highly correlated to SRH and to streamwise vorticity (ω_s) in the observed profiles is $\left|\overrightarrow{\omega}_h\right|$. Furthermore, $\left|\overrightarrow{\omega}_h\right|$ and $\left|\overrightarrow{SRF}\right|$ are themselves highly correlated due to their shared dependence on the hodograph length. The representative profiles produced by the SOMs were combined with a common thermodynamic profile to initialize quasi-realistic supercells in a cloud model. The simulations reveal that, across a range of real-world profiles, intense low-level mesocyclones are most closely linked to $\overrightarrow{\omega}_h$ and $\overrightarrow{SRF}$, while the angle between them appears to be mostly inconsequential.

Accepted for publication in *Journal of the Atmospheric Sciences*. DOI 10.1175/JAS-D-22-0253.1.

SIGNIFICANCE STATEMENT: About three-fourths of all tornadoes are produced by rotating thunderstorms (supercells). When the part of the storm near cloud base (approximately 1 km above the ground) rotates more strongly, the chance of a tornado dramatically increases. The goal of this study is to identify the simplest characteristic(s) of the environmental wind profile that can be used to forecast the likelihood of strong cloud base rotation. This study concludes that the most important ingredients for storm rotation are the magnitudes of the horizontal vertical wind shear between the surface–500 m and the storm inflow wind, irrespective of their relative directions. This finding may lead to improved operational identification of environments favoring tornado formation.

1. Introduction

The steps whereby a supercell produces a tornado (Davies-Jones 2015) may be delineated as: 1) the formation of a midlevel rotating updraft (i.e., via tilting of ambient environmental horizontal vorticity), 2) the generation of vertical vorticity (ζ_{sfc}) at or very close to the surface, and 3) the convergence and stretching of ζ_{sfc} into a tornado. Although this chain of processes is well-established, the successful discrimination between nontornadic and tornadic supercells has proven difficult operationally, as evident by a National Weather Service tornado warning false alarm rate of $\sim 75\%$ in the United States and a probability of detection asymptotically approaching 80% (Brotzge et al. 2011; Anderson-Frey et al. 2016). This difficulty is largely because both nontornadic and tornadic supercells have similar radar signatures (e.g., Blanchard and Straka 1998; Trapp 1999; Wakimoto and Cai 2000; Markowski et al. 2002, 2008, 2011; Klees et al. 2016; Coffer and Parker 2017).

There have been advances in identifying environments favorable for supercellular tornadoes including the creation of near-ground wind profile climatologies (e.g., Rasmussen and Blanchard 1998; Markowski et al. 2003; Thompson et al. 2003, 2007; Esterheld and Giuliano 2008; Thompson et al. 2012; Nowotarski and Jensen 2013; Nowotarski and Jones 2018; Warren et al. 2021). Storm-relative helicity (SRH) has been operationally used to characterize the amount of environmental rotation a storm can access as it matures (Davies-Jones et al. 1990). Physically, SRH represents the influx of streamwise environmental horizontal vorticity relative to an updraft's motion. While storms in high-SRH environments can be both tornadic and non-tornadic, we find that

Accepted for publication in *Journal of the Atmospheric Sciences*. DOI 10.1175/JAS-D-22-0253.1.

tornadic storms almost invariably have intense low-level dynamic lifting associated with strong mesocyclones (Coffer and Parker 2017, 2018; Coffer et al. 2017), and in turn that these strong mesocyclones are very closely linked to large ambient SRH. The 0–500 m AGL layer has the most practical relationship between SRH and the ability to discriminate between nontornadic and tornadic supercells (Coffer et al. 2019).

Historically, the dynamics associated with the production of ζ_{sfc} (i.e., step 2, as indicated above) have been emphasized (Davies-Jones and Brooks 1993; Rotunno and Klemp 1985; Wicker and Wilhelmson 1995; Adlerman et al. 1999; Markowski et al. 2008, 2012; Schenkman et al. 2014; Dahl 2015; Parker and Dahl 2015; Markowski 2016; Roberts et al. 2016; Roberts and Xue 2017; Roberts et al. 2020). However, Coffer and Parker (2017) showed that both nontornadic and tornadic supercells generate ample pre-tornadic ζ_{sfc}. The step that "makes or breaks" the mechanism of tornadogenesis is likely Step 3: the ability for ζ_{sfc} to be contracted into a tornado. Step 3 is most strongly favored when overlying rotation induces an upward pressure gradient acceleration that is capable of stretching ζ_{sfc} below the level of free convection (LFC) (e.g., Wicker and Wilhelmson 1995; Markowski and Richardson 2014; Coffer and Parker 2017; Orf et al. 2017; Yokota et al. 2018). This dynamic lifting and parent mesocyclone strength are strongly linked to the low-level environmental SRH (e.g., Markowski and Richardson 2014; Skinner et al. 2014; Coffer and Parker 2015, 2017, 2018; Coffer et al. 2017; Flournoy et al. 2020; Peters et al. 2020; Goldacker and Parker 2021). The particular importance of SRH very near the ground is supported by the finding that air parcel trajectories within the low-level mesocyclone[1] almost exclusively originate from below 300 m AGL in simulated supercells (Coffer and Parker 2017). Outflow buoyancy (i.e., surface cold pool density) also helps determine whether air parcels with ζ_{sfc} can be stretched and support the tornadogenesis process if reingested by the updraft (Markowski et al. 2002; Grzych et al. 2007; Markowski and Richardson 2014; Fischer and Dahl 2020). While storms themselves generate baroclinic horizontal vorticity, Coffer et al. (2022) showed that most of the vertical vorticity in the low-level mesocyclone originates from the environment. Given a cold pool of some intensity, we seek to understand the direct environmental influences that modulate the vertical velocity and vorticity below the near-cloud base mesocyclone.

[1]Here we define the low-level mesocyclone as being near cloud base of the parent storm, typically about 1 km AGL.

Accepted for publication in *Journal of the Atmospheric Sciences*. DOI 10.1175/JAS-D-22-0253.1.

A mathematical form of storm-relative helicity (SRH) is

$$SRH = \int_0^H \left| \overrightarrow{SRF} \right| \left| \overrightarrow{\omega}_h \right| \cos\phi \, dz, \tag{1}$$

where $\overrightarrow{SRF}$ is the storm-relative flow vector, $\overrightarrow{\omega}_h$ is the horizontal vorticity vector, ϕ is the angle between $\overrightarrow{SRF}$ and $\overrightarrow{\omega}_h$, and H is the top of the integration layer (dz) which for our study is 500 m AGL. Oftentimes, the quantity $\left| \overrightarrow{\omega}_h \right| \cos\phi$ is referred to as ω_s, or the horizontal streamwise vorticity. The comparative importance of the three SRH components to the low-level updraft and mesocyclone structure is murky. The observations of Coniglio and Parker (2020) revealed a correlation between tornadic environments and larger $\overrightarrow{SRF}$, however, the simulations of Peters et al. (2022) demonstrated that the low-level mesocyclone intensity (i.e., rotation) is modulated more strongly by ω_s than by $\left| \overrightarrow{SRF} \right|$ below 1 km. Both theory (Davies-Jones 1984; Davies-Jones and Brooks 1993; Davies-Jones 2015) and proximity soundings have highlighted the importance of ω_s to updraft rotation, but Davies-Jones (1984) further postulated that $\left| \overrightarrow{SRF} \right|$ must exceed 10 m s^{-1} with sufficient ω_s for updraft w and ζ to correlate. The differences among these various findings remain unexplained. The "critical-angle" (θ), defined between the 10 m AGL $\overrightarrow{SRF}$ and the 10–500 m AGL vertical wind shear vector ($\theta \approx \phi + 90^o$) has also shown some promise in tornado forecasting (Esterheld and Giuliano 2008). However, Coffer et al. (2019) and Coniglio and Parker (2020) have shown a lack of predictive skill for θ in larger datasets. Thus, the relative importance of $\left| \overrightarrow{\omega}_\mathrm{h} \right|$ vs. ϕ in producing large values of environmentally observed ω_s also remains unclear. *This spectrum of conclusions drives us to explore the following questions with respect to wind profiles commonly observed in nature*:

1. What combinations of $\left| \overrightarrow{\omega}_\mathrm{h} \right|$ and ϕ drive large values of ω_s?
2. What combinations of $\overrightarrow{\omega}_\mathrm{h}$ and $\overrightarrow{SRF}$ are typically observed and how are they related?
3. What are the relative influences of each SRH component on the development of low-level updraft rotation and potential for supercell tornadogenesis?

In pursuit of these questions, we attempt to identify the components' roles in determining the low-level updraft velocity and vorticity. We represent observed storm environments in nature utilizing self-organizing maps (SOMs) to characterize the distributions of the three SRH components. We then use the resultant SOM wind profiles as the basis for supercell simulations to quantify

Accepted for publication in *Journal of the Atmospheric Sciences*. DOI 10.1175/JAS-D-22-0253.1.

the direct impacts of each component on supercell characteristics and attendant tornadogenesis potential. Section 2 outlines the data and methods utilized in this study, Section 3 describes the results, and Section 4 provides a summary with suggestions for future investigations.

2. Data and Methods

a. Sounding Data

This study began with 20,194 near-storm proximity soundings that characterize right-moving supercell environments [previously utilized by Coffer et al. (2019) and Goldacker and Parker (2021)]. This dataset contains severe weather events from 2005–2015 for nontornadic supercells and from 2005–2017 for tornadic supercells (Coffer et al. 2019, their Fig. 1) and is an expanded version of that introduced by Smith et al. (2012) and Thompson et al. (2012). These soundings combine the Storm Prediction Center's mesoscale surface objective analysis (SFCOA, Bothwell et al. 2002) with model base-state isobaric data at 25 hPa intervals above the surface.

Events through April 2012 are constructed from the Rapid Update Cycle (RUC) model (Benjamin et al. 2004), and later events are constructed from the Rapid Refresh (RAP) model (Benjamin et al. 2016). Since the heights of isobaric levels are location dependent, we interpolated the profiles to heights above ground level (AGL) from 0–18 km with 50 m increments. To focus on variations within climatologically typical low-level hodograph shapes for right-moving supercells, only profiles with positive SRH (> 0 m^2 s^{-2}, thus requiring $\cos\phi > 0$) at every 50 m increment below 500 m AGL were retained. These 15,906 profiles served as the basis for our statistical analyses, SOMs, and subsequent simulations.

b. Self-organizing Maps

To sort and distill the 15,906 profiles, we used self-organizing maps (SOMs). SOMs are unsupervised machine learning tools that produce lattices of nodes (bins) containing the most prominent or recurring patterns in the dataset (e.g., Kohonen 1982, 1990, 1997). A number of recent studies have utilized this tool to distill large datasets of near-storm environmental profiles (e.g., Nowotarski and Jensen 2013; Anderson-Frey et al. 2017; Nowotarski and Jones 2018; Goldacker and Parker 2021; Warren et al. 2021). As in the study conducted by Goldacker and Parker (2021), we utilized the Python package MiniSom (Vettigli 2019). The SOMs were trained on two primary

Accepted for publication in *Journal of the Atmospheric Sciences*. DOI 10.1175/JAS-D-22-0253.1.

SRH ingredients; the 0–500 m $\left|\overrightarrow{SRF}\right|$ and $\left|\overrightarrow{\omega}_h\right|$ represented in 10 vertical layers of 50 m depth (i.e., from 0–500 m). The result is a 2-D lattice of 3x3 nodes, where the spatial arrangement of the nodes reveals the combined patterns in these two parameters[2] (Fig. 1). The constituent members within these nodes are distilled into node-averaged wind profiles for further analysis. The SOM procedure used an initialization via principal component analysis, a neighborhood radius of 0.28, a learning rate of 0.1, and 50,000 iterations so that every sample is selected at least three times to stabilize and minimize quantization and topographic errors (see Vettigli 2019; Goldacker and Parker 2021, for more details about these metrics).

To distill the third parameter's trend (ϕ), we then ordered each node's constituent members by ϕ and separated the order into terciles (lowest, middle, and highest 33%). This ordering and grouping approach spliced the original SOM lattice into three respective sub-lattices ($\mathcal{L}$, $\mathcal{M}$, and $\mathcal{U}$). The first sub-lattice ($\mathcal{L}$) has the most negative ϕ values, the third sub-lattice ($\mathcal{U}$) has the most positive ϕ values, and the second sub-lattice ($\mathcal{M}$) has intermediate ϕ values. The end result is 27 node-averaged wind profiles (nine each from sub-lattices $\mathcal{L}$, $\mathcal{M}$, and $\mathcal{U}$) that were used in our analysis and numerical simulations. For additional clarity, a key for the SOM node labels is provided in Fig. 2. The sub-lattices will be examined in detail in Section 3.

c. Environmental Profile Construction and Numerical Model Design

After initial analysis of the 27 SOM nodal wind profiles, we designed numerical experiments to identify storms' sensitivities to the differences among these profiles. The 27 wind profiles were combined with the VORTEX2 tornadic composite thermodynamic profile (Fig. 12 from Parker 2014) to initialize quasi-realistic supercell simulations. We utilized version 20.3 of the Bryan Cloud Model 1 (CM1) from Bryan and Fritsch (2002). The domain spanned 200 km in x, 200 km in y, and 18 km in z with a horizontal grid spacing of 250 m and a vertical grid spacing that stretched from 100 m below 1 km AGL to 250 m at and above 4.5 km. Coriolis and large-scale pressure gradient accelerations were neglected along with radiation and surface fluxes. A free-slip bottom boundary condition was selected since we are mainly interested in the macroscale low-level

[2]The 0–500 m individual zonal and meridional components of $\overrightarrow{SRF}$ $\left(\overrightarrow{SRF}_x\,,\,\overrightarrow{SRF}_y\right)$ and $\overrightarrow{\omega}_h$ $\left(\overrightarrow{\omega}_x\,,\,\overrightarrow{\omega}_y\right)$ were also tested as a training dataset. However, they produced a less distinctive sorting than the magnitudes of $\overrightarrow{SRF}$ and $\overrightarrow{\omega}_h$. $\overrightarrow{SRF}$ and $\overrightarrow{\omega}_h$ magnitudes were selected over u,v for the same reason, however, the sorting of the profiles based on u,v still displayed a correlation between 0–500 m SRH and the magnitude of $\overrightarrow{\omega}_h$ (which is identical to the 0–500 m bulk shear vector $\overrightarrow{S}$ magnitude) with no relationship between 0–500 m SRH and $\cos\phi$ (Fig.S1 in the Online Supplemental Materials).

Accepted for publication in *Journal of the Atmospheric Sciences*. DOI 10.1175/JAS-D-22-0253.1.

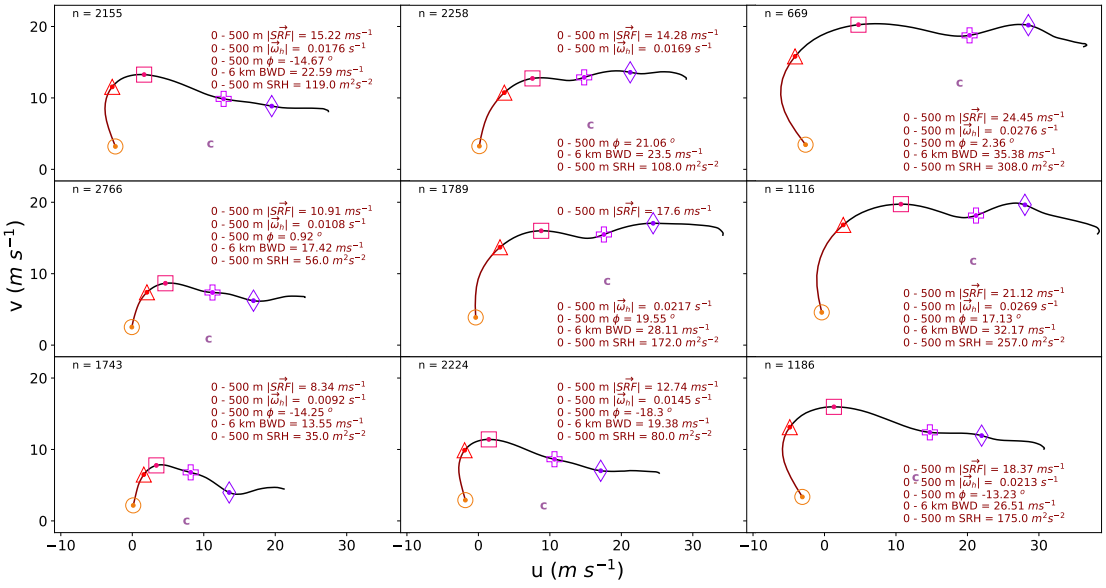

FIG. 1. The self-organizing map (SOM) lattice for the original nine recurring vertical wind structures trained on the 0–500 m $\left|\overrightarrow{SRF}\right|$ and $\left|\overrightarrow{\omega}_h\right|$ (which is the the collection of ten 50-m layers). The following levels AGL are noted: surface (0 m, orange circle), 500 m (red triangle), 1 km (pink square), 3 km (pink-purple plus), and 6 km (purple diamond). The profiles extend up to 12 km AGL, and storm motion is given by the symbol 'c' in red-purple. The first 500 m of the profile along with associated parameters of interest are colored in dark red. For this study, ϕ denotes the degree of rotation needed for the SRF vector to align with the ω_h vector. Positive (negative) values indicate a clockwise (counter-clockwise) rotation. The number of cases in each node are given by "n".

properties of supercells as a function of the vertical wind profile (as opposed to tornadogenesis itself). Microphysics were parameterized with the NSSL double-moment scheme with explicit graupel and hail density predictions (Mansell et al. 2010). The simulations were initialized with updraft nudging in the style of Naylor and Gilmore (2012) with a horizontal radius of 1 km, vertical centering at 1.5 km AGL with a radius of 1.5 km, and a maximum vertical velocity value (w) of 10 m s^{-1}. The nudging was at full strength for the first 15 minutes of the simulation and then ramped down to 0 m s^{-1} by 20 minutes. The domains were translated at the node-averaged Bunkers right-moving storm motion estimates (e.g., Bunkers et al. 2000, 2006; Zeitler and Bunkers 2005; Bunkers 2018) in congruence with the motions used in the SFCOA (Bothwell et al. 2002). These

Accepted for publication in *Journal of the Atmospheric Sciences*. DOI 10.1175/JAS-D-22-0253.1.

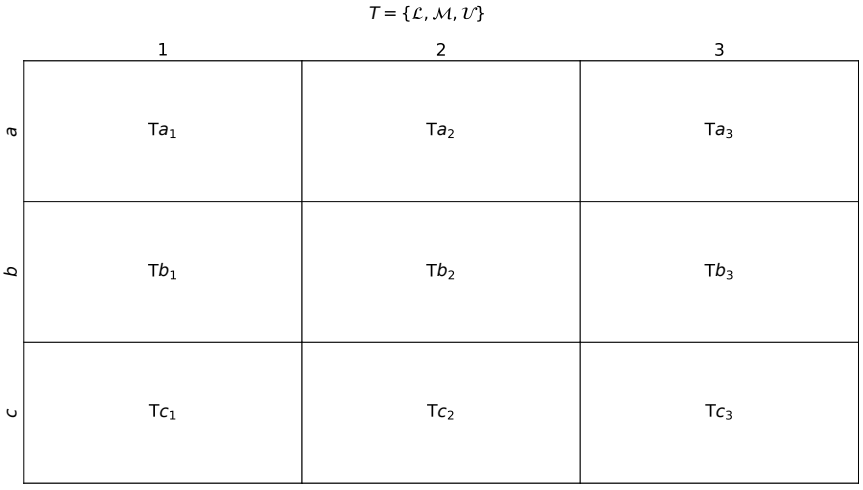

FIG. 2. A key for identifying the individual nodes within each of the SOM tercile lattices $\mathcal{L}$, $\mathcal{M}$, and $\mathcal{U}$.

storms were simulated for 2 hours, and we analyze the simulations from minutes 45 to 120 to remove the direct influences of the artificial forcing.

d. Proxies for Vertical Vorticity Stretching

Vertical motions beneath the near-cloud base mesocyclone facilitate "step 3" of tornadogenesis via the stretching of ζ_{sfc}, as shown by the inviscid, incompressible, Boussinesq vertical vorticity equation:

$$\frac{D\zeta}{Dt} = \underbrace{\left(\overrightarrow{\omega}_h \cdot \overrightarrow{\nabla}\right) w}_{\text{tilting}} + \underbrace{\zeta \left[\frac{\partial w}{\partial z}\right]}_{\text{stretching}}. \tag{2}$$

As discussed by Goldacker and Parker (2021), these vertical motions primarily arise from the low pressure associated with local rotation in a supercell's wind field. While buoyancy and irrotational contributions to the pressure field may also modulate these vertical motions, here we perform controlled experiments that focus on the specific role of the mesocyclone and associated vertical motions below the level of free convection. We analyze our results in terms of low-level ζ and w and seek to relate them to the components of our natural wind profiles.

Accepted for publication in *Journal of the Atmospheric Sciences*. DOI 10.1175/JAS-D-22-0253.1.

TABLE 1. Matrix Pearson Correlation Coefficient with the associated probabilities of observing each result if the correlation coefficient were 0 (p-values) for the 15,906 positive SRH cases utilizing each of the 50 m layers comprising the 0–500 m layer within each case. The form of each entry is (correlation coefficient , p-value).

	$\dot{SRH}$	$\left\lvert\dot{\overrightarrow{SRF}}\right\rvert$	$\lvert\dot{\vec{\omega}}_{\mathrm{h}}\rvert$	$\dot{\cos\phi}$	$\dot{\phi}$
$\dot{SRH}$	[1 , 0]	(0.597 , 0.0)	(0.872 , 0.0)	(-0.003 , 0.231)	(-0.032 , 0.0)
$\left\lvert\dot{\overrightarrow{SRF}}\right\rvert$		[1 , 0]	(0.347 , 0.0)	(-0.005 , 0.036)	(-0.104 , 0.0)
$\lvert\dot{\vec{\omega}}_{\mathrm{h}}\rvert$			[1 , 0]	(-0.001 , 0.754)	(0.045 , 0.0)
$\dot{\cos\phi}$				[1 , 0]	-
$\dot{\phi}$					[1 , 0]

3. Results

a. SRH Components in Nature

We designed the present study to understand hodographs commonly found in nature (the 15,906 near-storm profiles). Our first step was to identify the natural relationships[3] between $\left\lvert\overrightarrow{SRF}\right\rvert$, $\lvert\vec{\omega}_{\mathrm{h}}\rvert$, and $\cos\phi$. These relationships are encapsulated by SRH component correlation matrices. All 15,906 original profiles were first evaluated in 50 m layers for a total of 159,060 samples (each single layer variable denoted by ($\dot{\bullet}$) ; Table 1).

The correlation between $\dot{\mathrm{SRH}}$ and $\lvert\dot{\vec{\omega}}_{\mathrm{h}}\rvert$ is 0.872, the correlation between $\dot{\mathrm{SRH}}$ and $\left\lvert\dot{\overrightarrow{SRF}}\right\rvert$ is 0.597, and the correlation between $\dot{\mathrm{SRH}}$ and $\dot{\cos\phi}$ is a negligible -0.003. This immediately reveals that $\dot{\mathrm{SRH}}$ is most strongly linked to $\lvert\dot{\vec{\omega}}_{\mathrm{h}}\rvert$ within natural wind profiles. Interestingly, for these individual 50 m layers, the correlation between $\left\lvert\dot{\overrightarrow{SRF}}\right\rvert$ and $\lvert\dot{\vec{\omega}}_{\mathrm{h}}\rvert$ is only 0.347; we will see this relationship grow stronger as deeper layers and SOM nodal averages are considered.

---

[3]We also considered the following other combinations of SRH ingredients:

$$\omega_s = |\vec{\omega}_h| \cos\phi, \tag{3}$$

which is the streamwise horizontal vorticity or component of $\vec{\omega}_h$ aligned with $\overrightarrow{SRF}$,

$$SRF_s = \left|\overrightarrow{SRF}\right| \cos\phi, \tag{4}$$

which is the streamwise storm-relative flow or component of $\overrightarrow{SRF}$ aligned with $\vec{\omega}_h$, and

$$SRH_{max} = |\vec{\omega}_h|\,|\overrightarrow{SRF}|, \tag{5}$$

which represents the maximum SRH density possible in the presence of $\phi = 0^o$ (i.e., $\cos\phi = 1$), an idealized Beltrami flow. However, these formulations did not add information beyond the primary ingredients.

Accepted for publication in *Journal of the Atmospheric Sciences*. DOI 10.1175/JAS-D-22-0253.1.

TABLE 2. Matrix Pearson Correlation Coefficient with the associated probabilities of observing each result if the correlation coefficient were 0 (p-values) for the 15,906 positive SRH cases utilizing the integrated 0–500 m SRH and its average components within each case. The form of each entry is (correlation coefficient , p-value).

	SRH	$\left\lvert\overrightarrow{SRF}\right\rvert$	$\lvert\vec{\omega}_{\mathrm{h}}\rvert$	$\cos\phi$	ϕ
SRH	[1 , 0]	(0.737 , 0.0)	(0.908 , 0.0)	(-0.015 , 0.054)	(-0.115 , 0.0)
$\left\lvert\overrightarrow{SRF}\right\rvert$		[1 , 0]	(0.553 , 0.0)	(-0.018 , 0.025)	(-0.108 , 0.0)
$\lvert\vec{\omega}_{\mathrm{h}}\rvert$			[1 , 0]	(-0.011 , 0.18)	(-0.044 , 0.0)
$\cos\phi$				[1 , 0]	-
ϕ					[1 , 0]

We also examined the 0–500 m column integrals of SRH and its 0–500 m average components (Table 2), which are presumably more physically meaningful for low-level mesocyclone rotation than the individual 50 m layers.

The 0–500 m correlation between SRH and $\left\lvert\overrightarrow{\omega}_h\right\rvert$ is 0.908, the correlation between 0–500 m SRH and $\left\lvert\overrightarrow{SRF}\right\rvert$ is 0.737, and the correlation between 0–500 m SRH and $\cos\phi$ is still negligible (-0.015). The correlation between $\left\lvert\overrightarrow{SRF}\right\rvert$ and $\left\lvert\overrightarrow{\omega}_h\right\rvert$ is somewhat larger but still rather weak (0.553). To summarize, in nature, the relationships between SRH and its components as given by equation 1 are the strongest for SRH and $\left\lvert\overrightarrow{\omega}_h\right\rvert$ both when we maximize the sample size (i.e., 0–50 m layers), and when we consider the physically meaningful 0–500 m layer. In either case, $\cos\phi$ appears to be largely irrelevant. This highlights the primacy of $\left\lvert\overrightarrow{\omega}_h\right\rvert$ in scenarios where ω_s (i.e., $\left\lvert\overrightarrow{\omega}_h\right\rvert\cos\phi$) appears to be skillful (Peters et al. 2022). We also conclude that naturally observed values of $\left\lvert\overrightarrow{SRF}\right\rvert$ and $\left\lvert\overrightarrow{\omega}_h\right\rvert$ are not completely independent of one another. Later, we assess to what degree they can be considered separately.

We next examined the natural variability of these ingredients as encapsulated by the SOM sub-lattices, created by dividing each node of Fig. 1 into thirds in terms of ϕ. Distributions of the ϕ values within each of the original SOM nodes (Fig. 1) are presented in Fig. 3.

Notably, the distributions are not centered about 0^{o} in every node of the SOM. Clearly there is a high natural variability in ϕ within right-moving supercell environments. In all three resulting sub-lattices ($\mathcal{L}$: Fig. 4, $\mathcal{M}$: Fig. 5, and $\mathcal{U}$: Fig. 6), there are increases in 0–500 m $\left\lvert\overrightarrow{SRF}\right\rvert$, $\left\lvert\overrightarrow{\omega}_h\right\rvert$, and SRH from the bottom left panel (c_1) to the top right panel (a_3).

Accepted for publication in *Journal of the Atmospheric Sciences*. DOI 10.1175/JAS-D-22-0253.1.

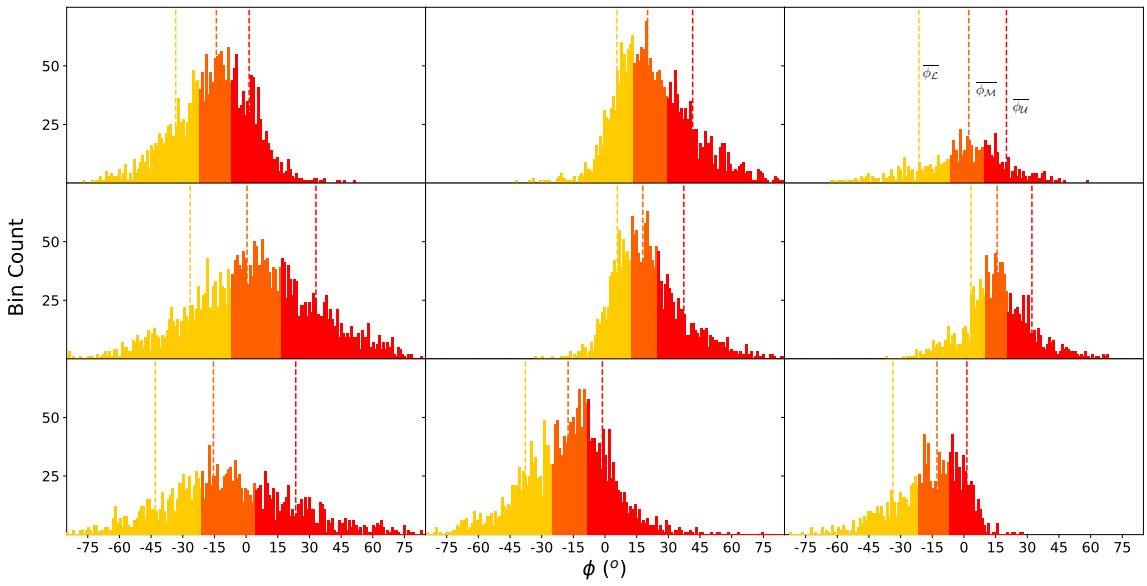

FIG. 3. Histograms corresponding to the distributions of ϕ within each of the co-located initial SOM nodes (Fig. 1). The lower tercile ($\mathcal{L}$) is given in yellow, the middle tercile ($\mathcal{M}$) is given in orange, and the upper tercile ($\mathcal{U}$) is given in red. Note that the width of the tercile bins for *each* initial SOM node are unique. The average ϕ value of each tercile is given in correspondingly colored lines (dashed). Note that bin widths for each tercile are related to the range in ϕ values within each tercile.

In sub-lattice $\mathcal{L}$, this diagonal trend (growth rate expressed as percent change) from (c_1) to (a_3) is greater in $\left|\overrightarrow{SRF}\right|$ than in $\left|\overrightarrow{\omega}_h\right|$. In sub-lattice $\mathcal{M}$, the trend is approximately equal in both $\left|\overrightarrow{SRF}\right|$ and $\left|\overrightarrow{\omega}_h\right|$. In sub-lattice $\mathcal{U}$, the trend is greater in $\left|\overrightarrow{\omega}_h\right|$ than in $\left|\overrightarrow{SRF}\right|$. These differing trends in percent change across the three sub-lattices enables us partly to assess the comparative influences of $\left|\overrightarrow{\omega}_h\right|$ and $\left|\overrightarrow{SRF}\right|$. The nodal values of SRH are also linked to both the Storm Prediction Center (SPC)'s categorized mesocyclone strengths (Smith et al. 2012) and the observed EF-scale tornado intensities (Figs. S2 and S3 in the Online Supplemental Materials, respectively).

We considered relationships between the 0–500 m SRH components for these 27 tercile hodographs. The nodal correlation between SRH and $\left|\overrightarrow{\omega}_h\right|$ is 0.982, the nodal correlation between SRH and $\left|\overrightarrow{SRF}\right|$ is 0.952, and the nodal correlation between SRH and cosϕ is 0.416 (Table 3).

By averaging the many hodographs within a node, some of the irregular features of natural profiles are smoothed out, improving the correlations. This effect is most notable in the dramatically inflated

Accepted for publication in *Journal of the Atmospheric Sciences*. DOI 10.1175/JAS-D-22-0253.1.

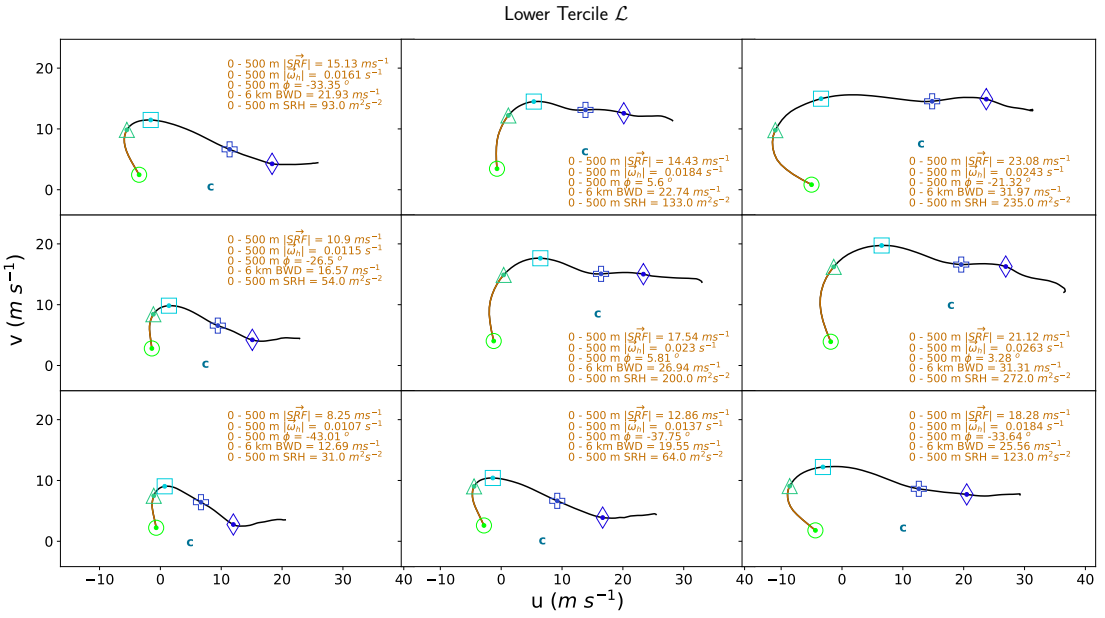

FIG. 4. As in Fig. 1 but for the lower tercile of ϕ values ($\mathcal{L}$). The following levels AGL are noted: surface (0 m, light green circle), 500 m (dark green triangle), 1 km (cyan square), 3 km (blue plus), and 6 km (indigo diamond). The profiles extend up to 12 km AGL, and storm motion is given by the symbol 'c' in teal. The first 500 m of the profile along with associated parameters of interest are colored in gold.

TABLE 3. Matrix Pearson Correlation Coefficient with the associated probabilities of observing each result if the correlation coefficient were 0 (p-values) for the 27 tercile environments (sub-lattices $\mathcal{L}$: Fig. 4, $\mathcal{M}$: Fig. 5, and $\mathcal{U}$: Fig. 6) utilizing the singular 0–500 m layer average data within each case as in Table2. The form of each entry is (correlation coefficient , p-value), and there are 27 total data points for each correlation coefficient measurement.

	SRH	$\left\lvert\overrightarrow{SRF}\right\rvert$	$\left\lvert\vec{\omega}_{\mathrm{h}}\right\rvert$	$\cos\phi$	ϕ
SRH	[1 , 0]	(0.952 , 0.0)	(0.982 , 0.0)	(0.416 , 0.031)	(0.268 , 0.177)
$\left\lvert\overrightarrow{SRF}\right\rvert$		[1 , 0]	(0.961 , 0.0)	(0.269 , 0.175)	(0.219 , 0.273)
$\left\lvert\vec{\omega}_{\mathrm{h}}\right\rvert$			[1 , 0]	(0.386 , 0.047)	(0.243 , 0.222)
$\cos\phi$				[1 , 0]	-
ϕ					[1 , 0]

correlation between $\left\lvert\overrightarrow{SRF}\right\rvert$ and $\left\lvert\vec{\omega}_h\right\rvert$ (0.961). While this high correlation is not present in the initial profiles, averaging reveals that the regularly occurring structures of hodographs do link $\left\lvert\vec{\omega}_h\right\rvert$

Accepted for publication in *Journal of the Atmospheric Sciences*. DOI 10.1175/JAS-D-22-0253.1.

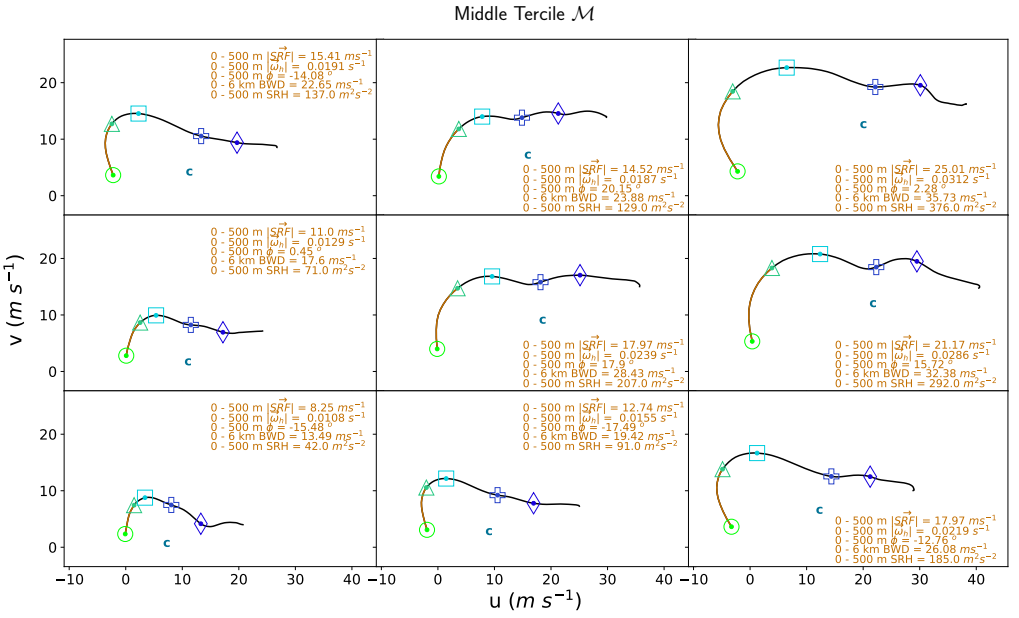

FIG. 5. As in Fig. 4 but for the middle tercile of ϕ values ($\mathcal{M}$).

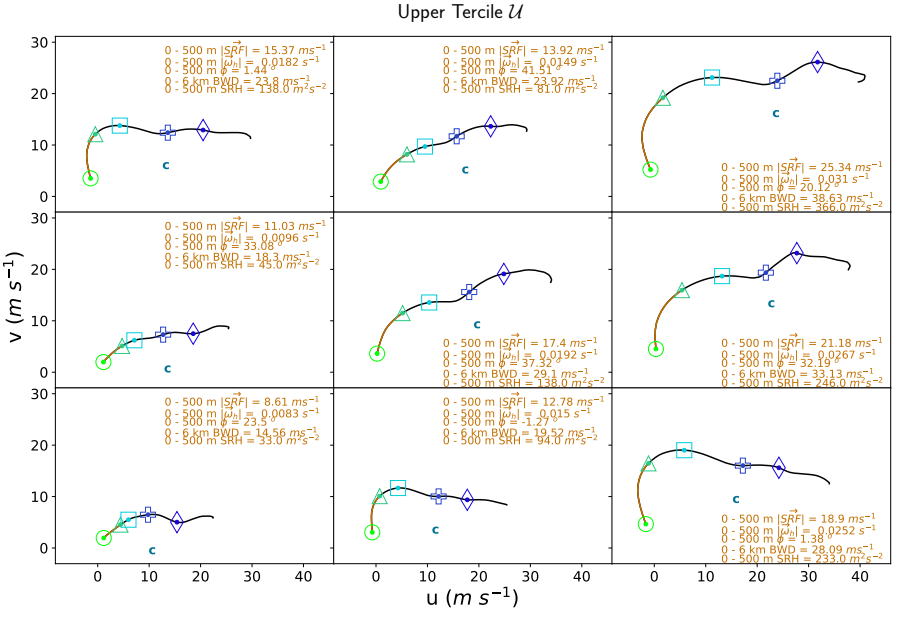

FIG. 6. As in Fig. 4 but for the upper tercile of ϕ values ($\mathcal{U}$).

and $\left|\overrightarrow{SRF}\right|$. Meanwhile, in the lowest 0–500 m of right-moving supercell wind profiles, $\left|\overrightarrow{\omega}_h\right|$ and

Accepted for publication in *Journal of the Atmospheric Sciences*. DOI 10.1175/JAS-D-22-0253.1.

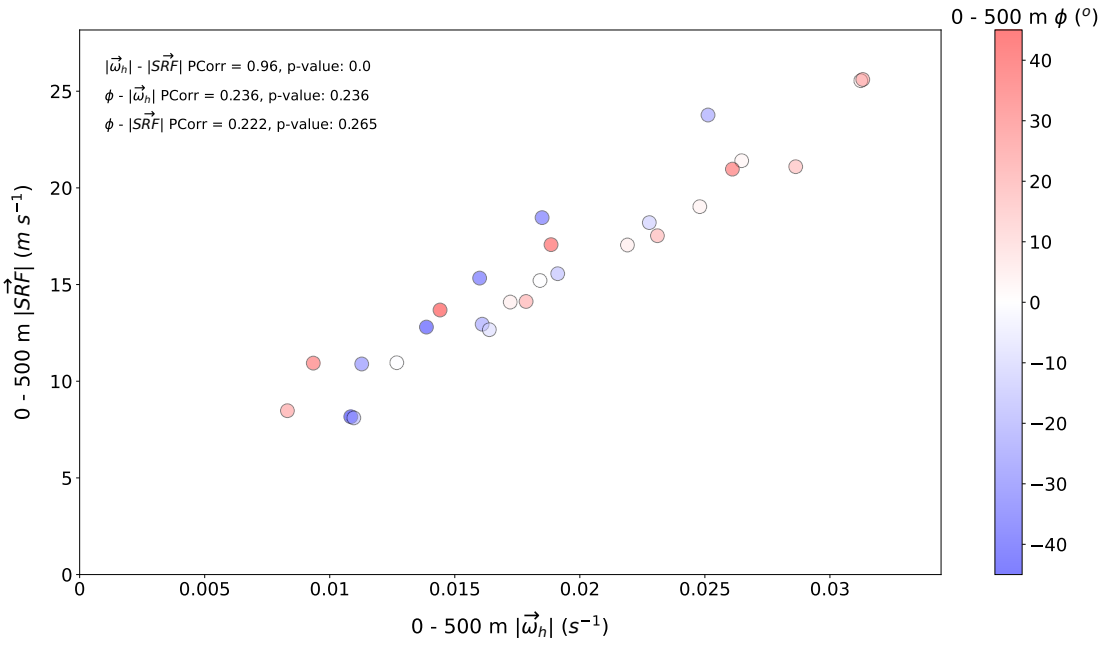

FIG. 7. Scatter plot showing the relationships between the 0–500 m SRH components $\left|\overrightarrow{\omega}_{\mathrm{h}}\right|$ (abscissa), $\left|\overrightarrow{SRF}\right|$ (ordinate), and ϕ (shaded). Pearson Correlation Coefficients (PCorr) and associated p-values are included.

$\left|\overrightarrow{SRF}\right|$ are uncorrelated from ϕ (Fig. 7). Thus, it appears that the strongest signals in supercell environments are associated with hodograph length[4] and not hodograph shape. The nodal profiles also reveal that ω_s is dominated by $\left|\overrightarrow{\omega}_h\right|$ (Fig. 8). Therefore, we hereafter focus primarily on $\left|\overrightarrow{\omega}_h\right|$ and not ω_s.

Obviously, $\left|\overrightarrow{\omega}_h\right|$, $\left|\overrightarrow{SRF}\right|$, and cos$\phi$ vary over rather different natural ranges. Therefore, we were interested in the degree to which the highest values of each ingredient were associated with the highest values of SRH. Thus, we analyzed percentiles of the SRH components relative to percentiles of SRH (Fig. 9, Table 3).

Again, for the nodal profiles, $\left|\overrightarrow{\omega}_h\right|$ is most closely linked to SRH while $\left|\overrightarrow{SRF}\right|$ is slightly less closely linked to SRH. We conclude that in nature, for right-moving supercell environments where SRH is large, both $\left|\overrightarrow{\omega}_h\right|$ and $\left|\overrightarrow{SRF}\right|$ are usually large. Meanwhile, cosϕ appears to exert comparatively little control over SRH even for the very highest values of SRH (Fig. 9). *In nature, ϕ appears to be the least deterministic component in the value of SRH*. This calls into question the

[4]Overall longer hodographs typically possess both larger low-level shear magnitudes, i.e. 0–500 m $\left|\overrightarrow{\omega}_h\right|$, and larger differences between mid-level winds (i.e., storm motion) and low-level winds (and thus larger $\left|\overrightarrow{SRF}\right|$).

Accepted for publication in *Journal of the Atmospheric Sciences*. DOI 10.1175/JAS-D-22-0253.1.

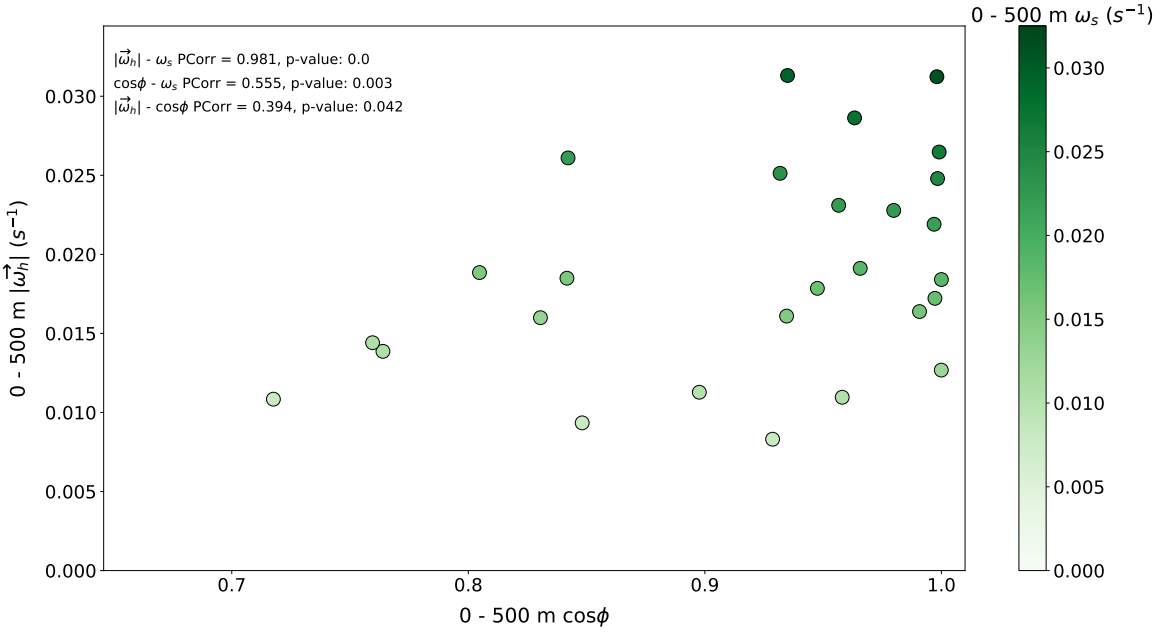

FIG. 8. Scatter plot showing the relationships between 0–500 m cosϕ (abscissa), $\left|\overrightarrow{\omega}_{\mathrm{h}}\right|$ (ordinate), and streamwise vorticity ω_s (shaded). Pearson Correlation Coefficients (PCorr) and associated p-values are included.

use of the "critical angle" (θ) in supercell and tornado forecasting (Esterheld and Giuliano 2008) since $\theta \approx \phi + 90^o$. The ineffectiveness of ϕ in modulating SRH demonstrated here extends to θ, in alignment with the findings of Coffer et al. (2019) and Coniglio and Parker (2020).

To directly evaluate the forecasting relevance of the SOM results, we examine the percentages of observed significant tornadoes [(E)F2+, ST], weak tornadoes [(E)F0–1, WT), and nontornadic supercells (NT) found in each of the 27 SOM nodes as a function of the nodal SRH, $\left|\overrightarrow{\omega}_h\right|$, $\left|\overrightarrow{SRF}\right|$, and cos$\phi$ (Fig. 10).

Tornado ratings do not necessarily directly represent low-level mesocyclone (or even tornado) intensity, but there is high confidence that STs represent correctly identified tornadoes versus other wind damage events (e.g., Brooks et al. 2003). Given the diversity of profiles found within each node, even the most favorable environments contain at most 30% STs. Even so, it is again telling that cosϕ has a very weak relationship to the probability that an ST was observed in a given environment. In contrast, the correlations to other SRH components (e.g., $\left|\overrightarrow{\omega_h}\right|$ and $\left|\overrightarrow{SRF}\right|$) are much larger.

Accepted for publication in *Journal of the Atmospheric Sciences*. DOI 10.1175/JAS-D-22-0253.1.

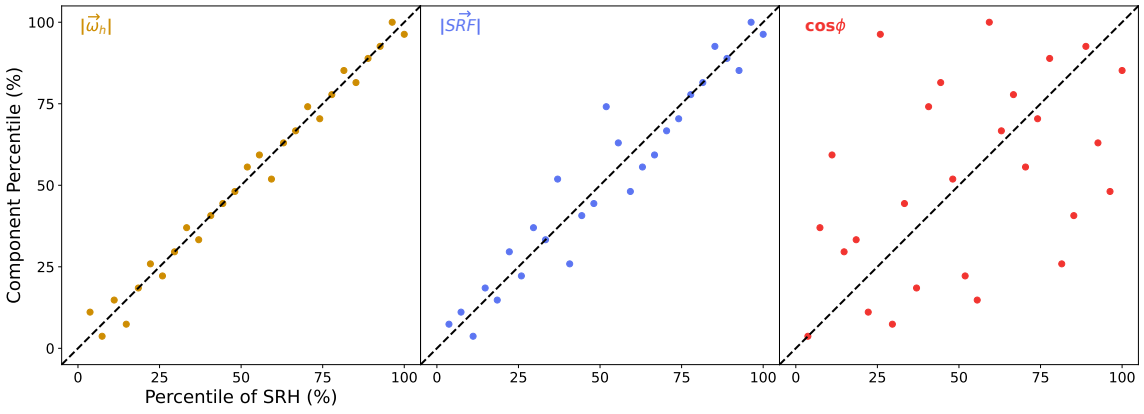

FIG. 9. Scatter plots for the percentiles of 0–500 m SRH (m^2 s^{-2}, abscissa) compared to 0–500 m SRH components [$\left|\overrightarrow{\omega}_{\mathrm{h}}\right|$ (s^{-1}, gold), $\left|\overrightarrow{SRF}\right|$ (m s^{-2}, indigo), and cosϕ (bright red); for the 27 tercile environments. A 1:1 ratio line is provided for reference in dashed black. The Pearson Correlation Coefficients and associated p-values [of the form (PCorr, p-value) are (0.992, 0.0) for $\left|\overrightarrow{\omega}_{\mathrm{h}}\right|$ and SRH, (0.963, 0.0) for $\left|\overrightarrow{SRF}\right|$ and SRH, and (0.436, 0.023) for cosϕ and SRH.

Coffer and Parker (2017) demonstrated how horizontal crosswise vorticity (ω_c) could theoretically be detrimental to "step 3" of tornadogenesis, however, Coffer et al. (2019) and Goldacker and Parker (2021, their Fig. 18) showed that while this deleterious effect may be present, there is no skill in predicting the strength of the low-level mesocyclone based on ω_c alone. The other component of the horizontal vorticity (ω_s) has proven useful in this regard. Coffer et al. (2019), Peters et al. (2020), and Peters et al. (2022) have all identified the primary role of ω_s in governing low-level mesocyclone strength and possible tornadogenesis. Here, we demonstrate the primacy of $\left|\overrightarrow{\omega}_h\right|$ over cosϕ within ω_s. Based on this analysis of natural hodographs, it is tempting to declare that $\left|\overrightarrow{\omega}_h\right|$ is the most important SRH ingredient to mesocyclone growth. However, to thoroughly investigate this claim, we seek to identify how these natural correlations correspond to explanatory dynamical relationships. We therefore turn to numerical experiments next.

Accepted for publication in *Journal of the Atmospheric Sciences*. DOI 10.1175/JAS-D-22-0253.1.

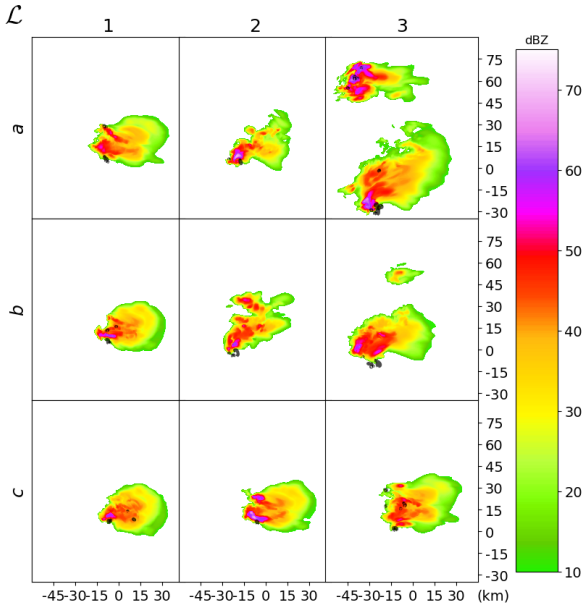

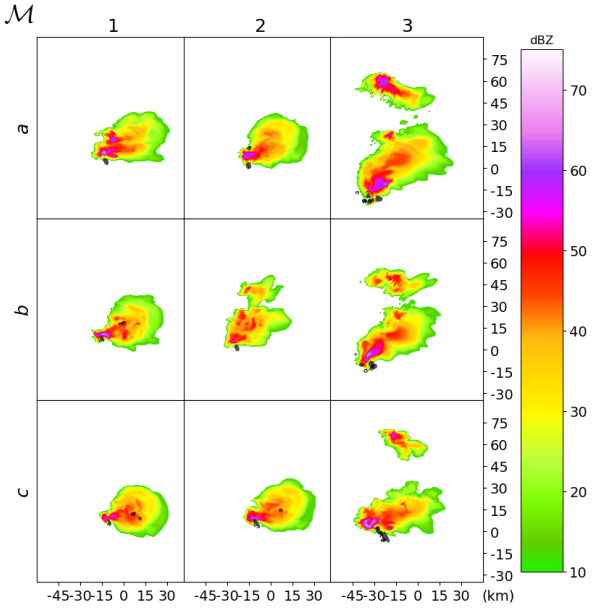

Accepted for publication in *Journal of the Atmospheric Sciences*. DOI 10.1175/JAS-D-22-0253.1.

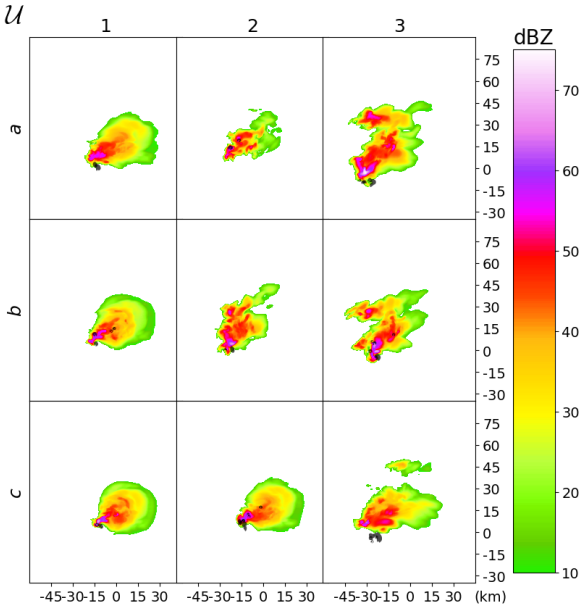

FIG. 11. A schematic of the 1 km simulated reflectivity (dBZ) for each simulation within sub-lattices $\mathcal{L}$, $\mathcal{M}$, and $\mathcal{U}$ at the time of maximum storm intensity as designated by the simulation maximum in 0–3 km updraft helicity (UH). Associated times and UH values are located in Table 4. The 1 km updraft helicity density (UH_D) is contoured in black at 0.1 m s^{-2}.

Accepted for publication in *Journal of the Atmospheric Sciences*. DOI 10.1175/JAS-D-22-0253.1.

TABLE 4. The tercile simulations and their corresponding time of maximum intensity [proxied by 0–3 km updraft helicity UH in minutes] along with the value of maximum 0–3 km UH (UH_{max}). The 0–3 km UH is presented as a 1 km radially averaged value about the single pixel maximum. The 0–6 km bulk wind difference (BWD), 0–500 m storm-relative helicity (SRH), and accompanying SRH components ($\left|\overrightarrow{SRF}\right|$, and $\left|\overrightarrow{\omega}_h\right|$, and $\cos\phi$ with original ϕ).

Simulation	Time of Maximum 0–3 km UH (min)	UH_{max} ($m^2\ s^{-2}$)	0–6 km BWD ($m\ s^{-1}$)	0–500 m SRH ($m^2\ s^{-2}$)	0–500 m $\left\|\overrightarrow{SRF}\right\|$ ($m\ s^{-1}$)	0–500 m $\left\|\overrightarrow{\omega}_h\right\|$ (s^{-1})	0–500 m $\cos\phi$	0–500 m ϕ (°)
$\mathcal{L}a1$	51	1173	21.9	93	15	0.016	0.835	-33
$\mathcal{L}a2$	67	885	22.7	133	14	0.018	0.995	6
$\mathcal{L}a3$	117	3088	32	235	23	0.024	0.932	-21
$\mathcal{L}b1$	45	717	16.6	54	11	0.012	0.895	-27
$\mathcal{L}b2$	76	1609	26.9	200	18	0.023	0.995	6
$\mathcal{L}b3$	120	1717	31.3	272	21	0.026	0.998	3
$\mathcal{L}c1$	46	364	12.7	31	8	0.011	0.731	-43
$\mathcal{L}c2$	45	1147	19.6	64	13	0.014	0.791	-38
$\mathcal{L}c3$	51	1384	25.6	123	18	0.018	0.833	-34
$\mathcal{M}a1$	52	1920	22.6	137	15	0.019	0.97	-14
$\mathcal{M}a2$	46	1415	23.9	129	15	0.019	0.939	20
$\mathcal{M}a3$	104	3790	35.7	376	25	0.031	0.999	2
$\mathcal{M}b1$	53	845	17.6	71	11	0.013	1	0
$\mathcal{M}b2$	95	995	28.4	207	18	0.024	0.952	18
$\mathcal{M}b3$	104	2693	32.4	292	21	0.029	0.963	16
$\mathcal{M}c1$	45	224	13.5	42	8	0.011	0.964	-15
$\mathcal{M}c2$	45	1109	19.4	91	13	0.016	0.954	-17
$\mathcal{M}c3$	120	2146	26.1	185	18	0.022	0.975	-13
$\mathcal{U}a1$	47	1442	23.8	138	15	0.018	1	1
$\mathcal{U}a2$	70	504	23.9	81	14	0.015	0.749	42
$\mathcal{U}a3$	81	2291	38.6	366	25	0.031	0.939	20
$\mathcal{U}b1$	50	545	18.3	45	11	0.01	0.838	33
$\mathcal{U}b2$	80	657	29.1	138	17	0.019	0.795	37
$\mathcal{U}b3$	73	1125	33.1	246	21	0.027	0.846	32
$\mathcal{U}c1$	45	265	14.6	33	9	0.008	0.917	24
$\mathcal{U}c2$	46	1181	19.5	94	13	0.015	1	-1
$\mathcal{U}c3$	104	1613	28.1	233	19	0.025	1	1

All of the simulated storms are supercells (i.e., possessing hook echoes, weak echo regions, mesocyclones, and updraft helicity at 1 km AGL). Our analysis focuses on the low-level mesocyclone, hence we explore the linkage of each SRH ingredient to the evolution of 0–1 km w and ζ. Our simulated low-level mesocyclone growth indeed increases with 0–500 m SRH as expected

Accepted for publication in *Journal of the Atmospheric Sciences*. DOI 10.1175/JAS-D-22-0253.1.

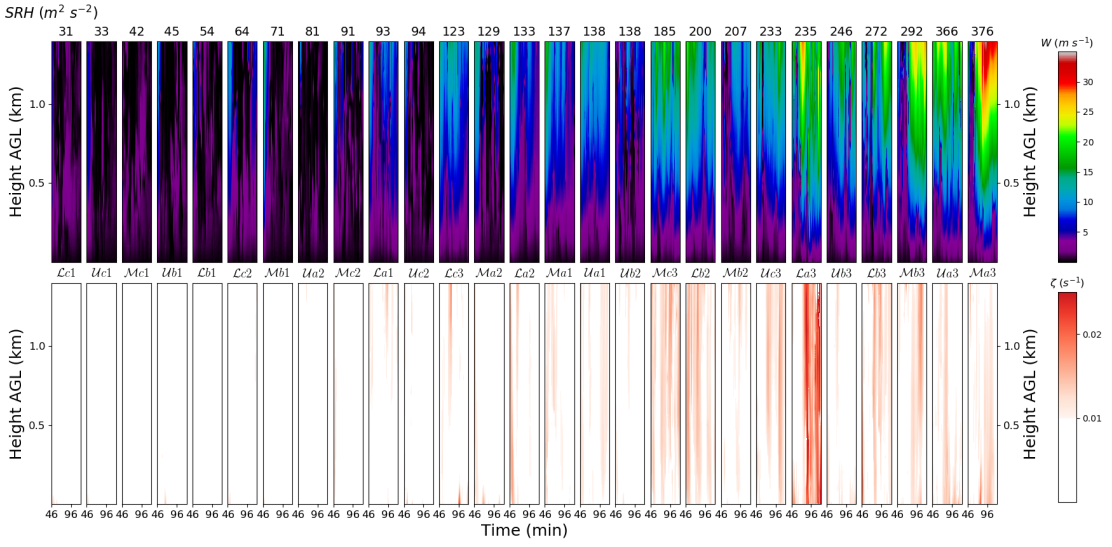

Fig. 12. Time-height plots displaying 0–1 km vertical velocity w (top) and vertical vorticity ζ values (bottom) within the center of the low-level updraft for all 27 SOM node simulations. The simulation label is provided between the top and bottom plots. The simulations are arranged in ascending order of 0–500 m SRH (label top left).

(Fig. 12). We note that this trend is largely similar to those for ascending values of $\left|\overrightarrow{\omega}_h\right|$ (Fig. 13) and $\left|\overrightarrow{SRF}\right|$ (Fig. 14). If ϕ was an explanatory variable for low-level mesocyclone intensification, we would expect to see the largest w and ζ values below 1 km AGL as ϕ approaches 0° (i.e., cosϕ = 1). However, Fig. 15 lacks a congregation of the robust 0–1 km w and ζ evolutions about 0°. The strongest low-level simulated w and ζ are associated with $\mathcal{L}a_3$, $\mathcal{M}a_3$, $\mathcal{M}b_3$, and $\mathcal{U}a_3$ corresponding to ϕ values of –21°, 2°, 16°, and 20° with cosϕ values of 0.93, 1.0, 0.96, and 0.94, respectively, with additional environments of cosϕ = 1.0 failing to promote strong w and ζ (e.g., $\mathcal{M}b_1$). We seek to distill these visual trends by quantifying the potential for stretching by the low-level mesocyclone across these 27 simulations.

Updraft helicity density (UH$_D$ or ζw) is shown at 1 km AGL to characterize the footprint of the strongest low-level mesocyclones. The strongest pockets of ζw in excess of 0.4 m s^{-2} occur only where $\left|\overrightarrow{\omega}_h\right|$ and $\left|\overrightarrow{SRF}\right|$ are the largest. Meanwhile, these environments producing strong ζw have widely varying values of ϕ (Fig. 16; $\mathcal{L}a_3$ = –21°, $\mathcal{L}b_3$ = 3°, $\mathcal{L}c_3$ = –34°, $\mathcal{M}a_3$ = 2°, $\mathcal{M}b_3$ = 16°, $\mathcal{M}c_3$ = –13°, $\mathcal{U}a_3$ = 20° $\mathcal{U}b_3$ = 32°, and $\mathcal{U}c_3$ = 0°).

Accepted for publication in *Journal of the Atmospheric Sciences*. DOI 10.1175/JAS-D-22-0253.1.

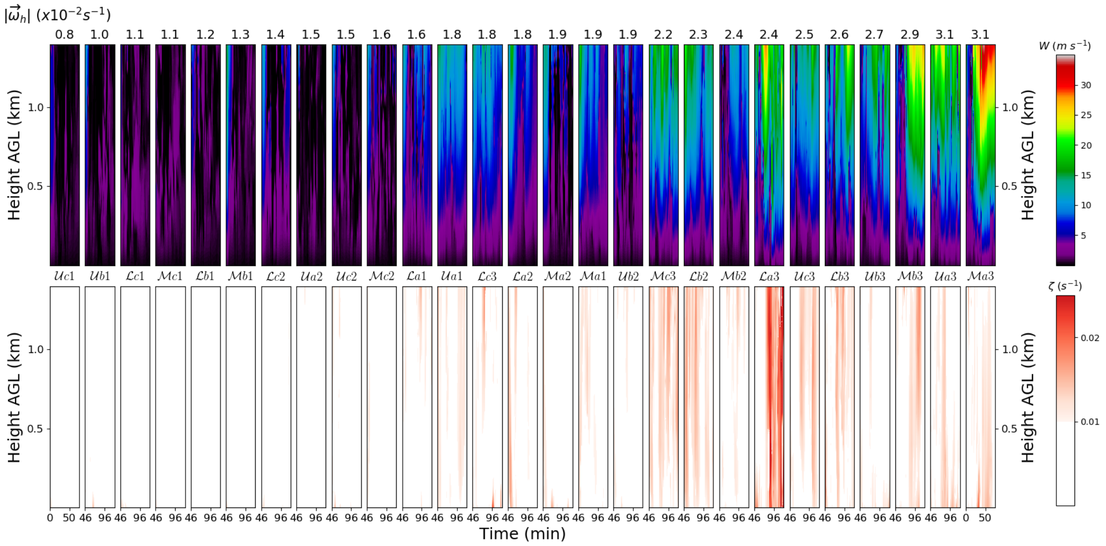

FIG. 13. As in Fig. 12 but arranged in ascending order of $\left|\overrightarrow{\omega}_{\mathrm{h}}\right|$.

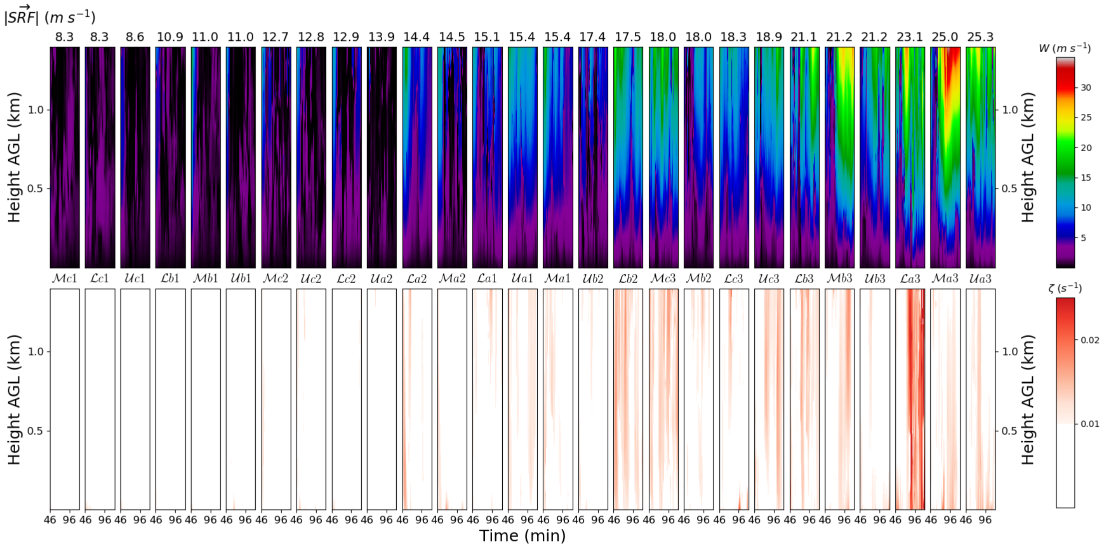

FIG. 14. As in Fig. 12 but arranged in ascending order of $\left|\overrightarrow{SRF}\right|$.

Accepted for publication in *Journal of the Atmospheric Sciences*. DOI 10.1175/JAS-D-22-0253.1.

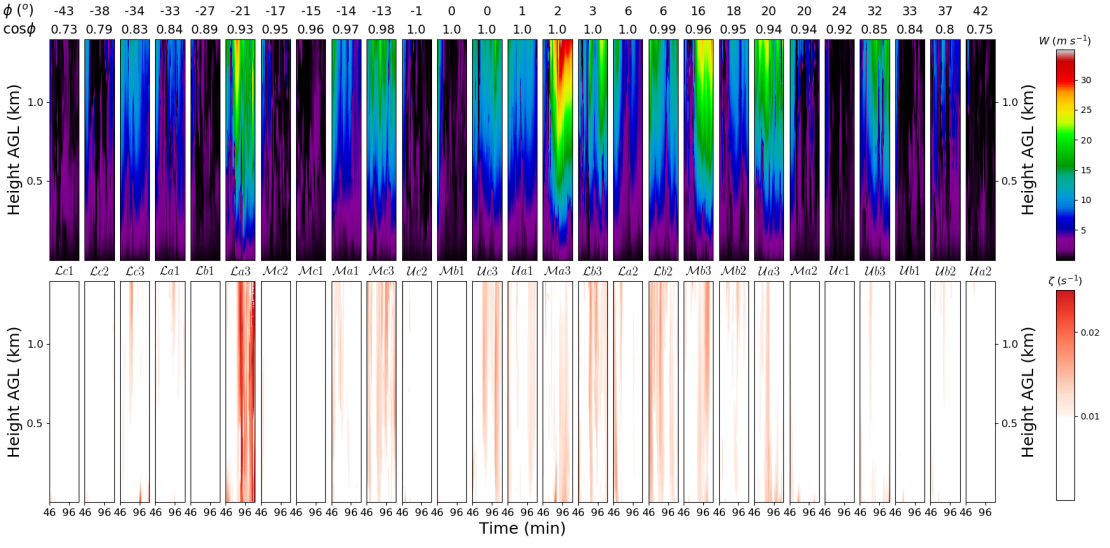

FIG. 15. As in Fig. 12 but arranged in ascending order of ϕ. The associated value of cosϕ is also reported at the top of each column.

Accepted for publication in *Journal of the Atmospheric Sciences.* DOI 10.1175/JAS-D-22-0253.1.

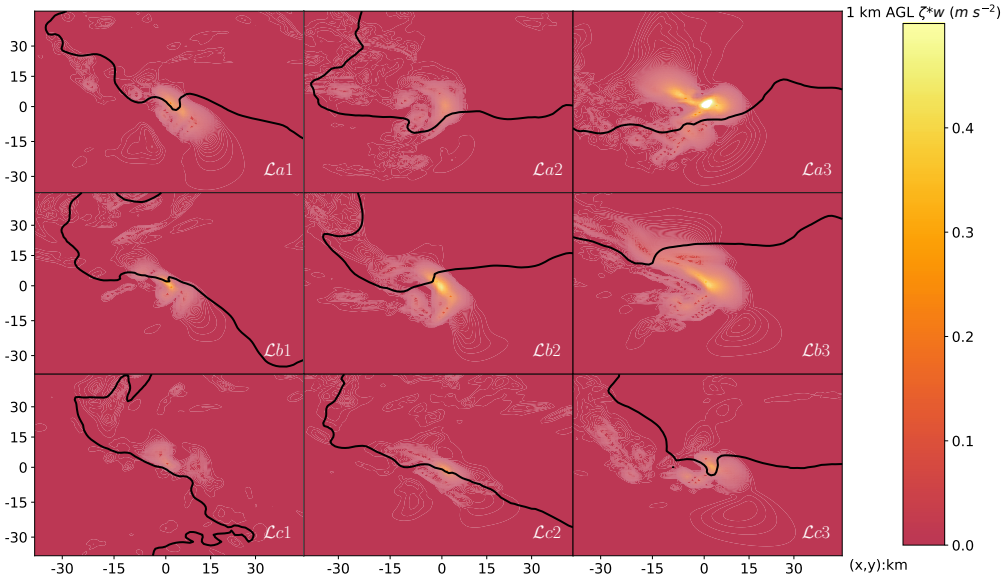

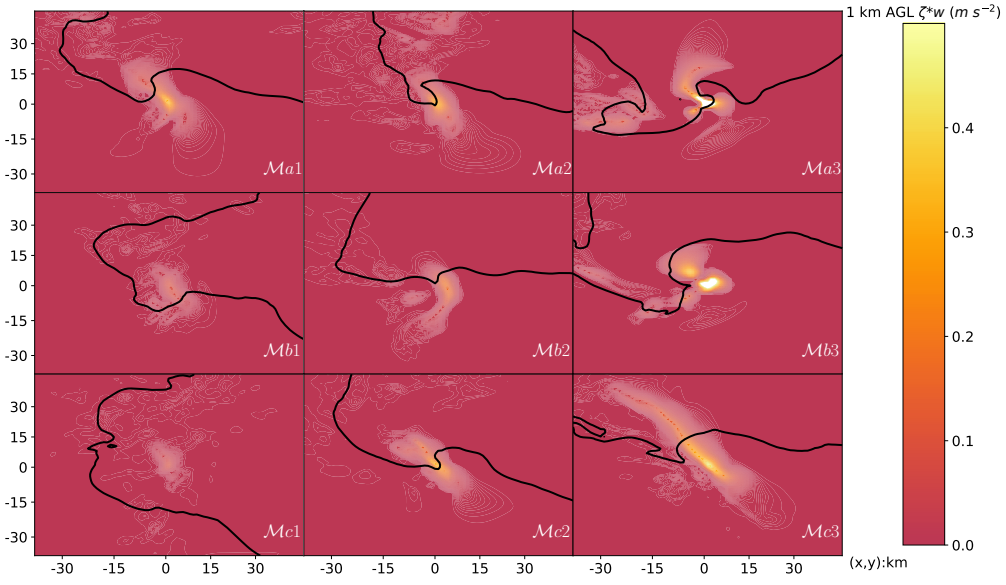

Accepted for publication in *Journal of the Atmospheric Sciences*. DOI 10.1175/JAS-D-22-0253.1.

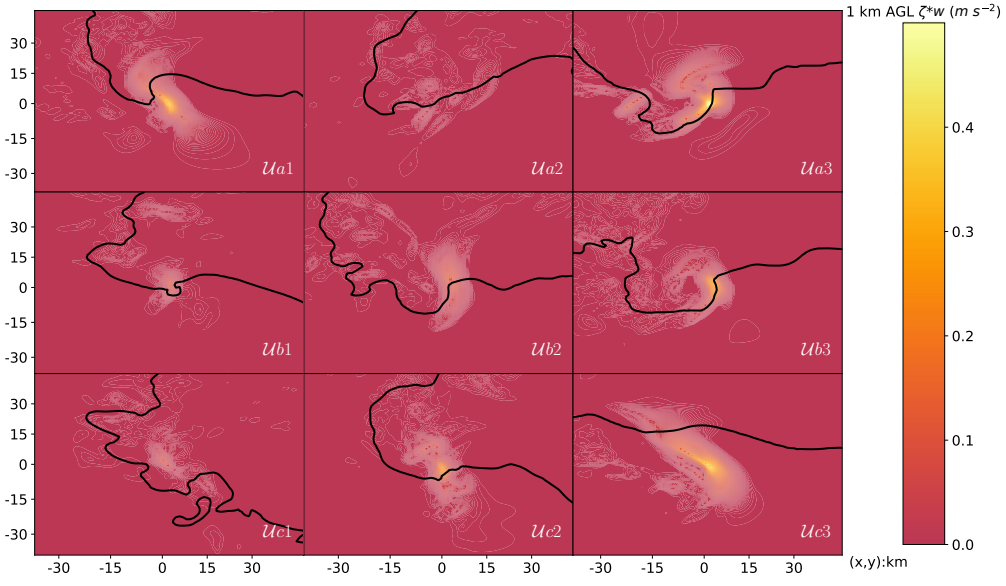

FIG. 16. A plan view of 1 km AGL updraft helicity density (ζw, shaded) along with the 10 dBZ simulated reflectivity contour (solid black) for each simulation within sub-lattices $\mathcal{L}$, $\mathcal{M}$, and $\mathcal{U}$. This plan view presents 10-minute averages centered at the time of maximum 0–3 km UH intensity (Table 4). Environment designations are located in the bottom right corner of each node.

Accepted for publication in *Journal of the Atmospheric Sciences*. DOI 10.1175/JAS-D-22-0253.1.

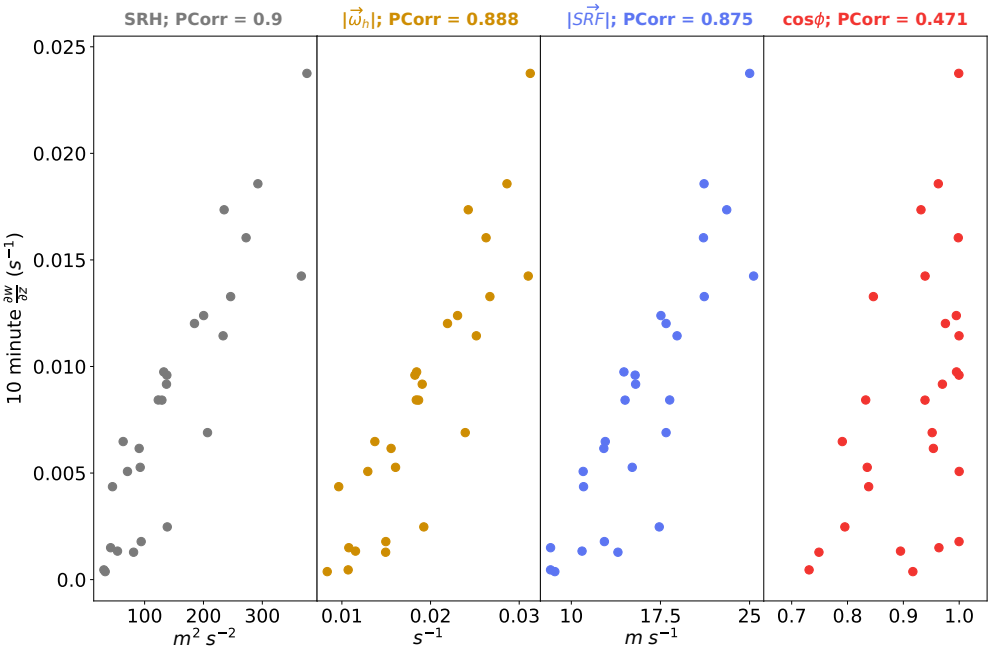

FIG. 17. Scatter plots illustrating the relationships between the 10-minute persistent 0–1 km stretching proxy $\frac{\partial w}{\partial z}$ (s^{-1}) against 0–500 m SRH (silver), $\left|\vec{\omega}_{\mathrm{h}}\right|$ (gold), $\left|\overrightarrow{SRF}\right|$ (indigo), and cosϕ (bright red). The Pearson Correlation Coefficient (PCorr) is provided, and all p-values are 0.0 except for the correlation between $\frac{\partial w}{\partial z}$ and cosϕ (0.013).

We next examined the highest consistently observed $\frac{\partial w}{\partial z}$ values for periods as short as 1 minute and as long as 45 minutes. We found that $\frac{\partial w}{\partial z}$ would typically remain large for a period of approximately 10 minutes during the prime window for tornadogenesis (see Fig. S4 in the Online Supplemental Materials) which agrees well with the tornadogenesis periods found in prior studies (5–15 minutes suggested by Davies-Jones et al. 2001; Clark et al. 2021). We correlated the highest continuously-produced 10-minute $\frac{\partial w}{\partial z}$ value with the SRH components. While the correlations between $\frac{\partial w}{\partial z}$ and SRH, $\frac{\partial w}{\partial z}$ and $\left|\vec{\omega}_h\right|$, and $\frac{\partial w}{\partial z}$ and $\left|\overrightarrow{SRF}\right|$ are extremely similar (0.9, 0.888, 0.875, respectively), the correlation between $\frac{\partial w}{\partial z}$ and cosϕ is only 0.471 (Fig. 17).

It seems clear that, in nature, cosϕ is the least influential component of the SRH and ω_s. Both $\left|\vec{\omega}_h\right|$ and $\left|\overrightarrow{SRF}\right|$ appear to be quite influential, and it is unclear which of the two might be more physically consequential because they are so well-correlated. More idealized hodographs such as

Accepted for publication in *Journal of the Atmospheric Sciences*. DOI 10.1175/JAS-D-22-0253.1.

those studied by Peters et al. (2022) may lead to clearer attribution, but it seems that in nature these ingredients largely covary.

4. Conclusion

a. Summary and Results

Recent research has narrowed focus on the importance of near-ground environmental vertical wind shear to supercell tornadogenesis. One of the most physically meaningful and operationally relevant parameters is the 0–500 m storm-relative helicity (SRH), which includes storm-relative flow magnitude $\left| \overrightarrow{SRF} \right|$, environmental horizontal vorticity magnitude $\left| \overrightarrow{\omega}_h \right|$, and the angle between the vectors ϕ (appearing in SRH as $\cos\phi$). We have examined the relationships among these ingredients as well as their role in modulating the potential stretching of ζ_{sfc}. We specifically focus on naturally occurring environments of right-moving supercells, and our primary findings are as follows:

- In natural wind profiles, the 0–500 m SRH and ω_s are both most strongly correlated to $\left| \overrightarrow{\omega}_h \right|$, not $\cos\phi$ or ϕ. In nature, we do not frequently observe environments where SRH or ω_s are small because large $\left| \overrightarrow{\omega}_h \right|$ occurs in conjunction with small $\cos\phi$.
- Self-organizing maps (SOMs) reveal that, on average, $\left| \overrightarrow{\omega}_h \right|$ and $\left| \overrightarrow{SRF} \right|$ are highly correlated due to their shared dependence on hodograph length and not hodograph shape.
- In simulated supercells within the natural environments studied here, $\left| \overrightarrow{\omega}_h \right|$ and $\left| \overrightarrow{SRF} \right|$ are well-correlated to low-level mesocyclone growth and potential stretching, whereas ϕ, $\cos\phi$, and the related critical angle ($\theta \approx \phi + 90^{\circ}$) have minimal predictive power.

b. Future Work

The roles of $\left| \overrightarrow{SRF} \right|$ and $\left| \overrightarrow{\omega}_{\mathrm{h}} \right|$ on low-level mesocyclone intensity are not fully separable in the present dataset. However, our results support the claim that the least relevant parameter to low-level mesocyclone evolution is the 0–500 m ϕ (or $\cos\phi$). Prior to wind profile averaging and smoothing, we also find that $\left| \overrightarrow{\omega}_{\mathrm{h}} \right|$ is more closely related to SRH than is $\left| \overrightarrow{SRF} \right|$ (although this advantage seemingly disappears after profiles are averaged). In light of the claim by Peters et al. (2022) that ω_s predominates over $\left| \overrightarrow{SRF} \right|$ in determining the character of supercells and mesocyclones, this might

Accepted for publication in *Journal of the Atmospheric Sciences*. DOI 10.1175/JAS-D-22-0253.1.

mean that $\left|\overrightarrow{\omega}_{\mathrm{h}}\right|$ is the most important tornado forecasting parameter. To the extent that $\left|\overrightarrow{\omega}_{\mathrm{h}}\right|$ and $\left|\overrightarrow{SRF}\right|$ covary (and that both outperform ϕ and cosϕ), this would support the primary importance of hodograph length over hodograph shape as a forecasting consideration. We encourage the continued testing of such alternative approaches. Unfortunately, as expressed by Coffer et al. (2020), there is typically inadequate sampling of kinematic profiles in the lowest 500 m AGL. Many of our best operational datasets are beholden to model boundary layer parameterizations in this layer. Given the great societal importance of tornado forecasting and warning, we strongly encourage the field to pursue development of networks of low-cost, sustainable, non-expendable sensors that can be repeatably used to measure the low-level (minimally 0–500 m AGL) wind profile.

Beyond these ramifications, the following questions logically arise:

1. Beyond the direct effects of SRH on the mesocyclone, what are the other within-storm differences (e.g., precipitation arrangement, cold pool properties, etc.) that accompany this range of supercell wind profiles?

2. While the present results (using Bunkers et al. (2000) right-moving storm motion vector) can be applied even prior to storm formation, what are the possible impacts of observed storm motions that deviate substantially from the Bunkers estimate?

3. What meso- or synoptic scale settings combine to produce the types of wind profiles in which both 0–500 m $\overrightarrow{\omega}_{\mathrm{h}}$ and $\overrightarrow{SRF}$ are large? Are these wind profiles unique to particular regions or seasons? Are certain thermal profiles linked to these unique wind profiles?

4. What are the independent physical impacts of $\left|\overrightarrow{\omega}_{\mathrm{h}}\right|$ and $\left|\overrightarrow{SRF}\right|$ on low-level mesocyclone development and low-level vertical vorticity stretching?

The first two questions could potentially be addressed with a dataset like the current 27 storm simulations. The third question could potentially be addressed with meso- and synoptic scale climatologies for environments where $\left|\overrightarrow{SRF}\right|$ and $\left|\overrightarrow{\omega}_{h}\right|$ are large. The fourth question could potentially be addressed using idealized cloud model simulations with wind profiles that minimize changes in one component while maximizing changes in the other component. The present study is unique in the perspective of analyzing supercell updraft properties and attributing them to SRH components *found in nature*, and our findings could spawn more effective techniques for

Accepted for publication in *Journal of the Atmospheric Sciences*. DOI 10.1175/JAS-D-22-0253.1.

interrogating environmental hodographs when making forecasts for potentially tornadic supercells and targeting future modeling experiments.

Accepted for publication in *Journal of the Atmospheric Sciences*. DOI 10.1175/JAS-D-22-0253.1.

Acknowledgments. We would like to thank the NCSU Convective Storms Group members Dr. Brice Coffer, Adam Werkema, Miranda Silcott, Zachary Chalmers, Sean Melanson, and Matt Burich for their valuable opinions and unique perspectives on experimental approach and graphic design. We would also like to thank three anonymous reviewers for their constructive feedback and Dr. Johannes Dahl for editorial support. The lead author would also like to thank Dr. Sandra Yuter, Katherine Hollinger and Cameron Masiello for fruitful discussions and data presentation ideas. This study was supported by NSF Grant AGS-1748715. We thank Dr. George Bryan for his continued support of CM1 and to NCAR for their computing services (Cheyenne, doi:10.5065/D6RX99HX).

Data availability statement. Self-organizing map (SOM) lattice profiles, input soundings, and model configuration files for the simulations presented in this study are available from https://doi.org/10.5061/dryad.f1vhhmh1f.

Accepted for publication in *Journal of the Atmospheric Sciences*. DOI 10.1175/JAS-D-22-0253.1.

References

Adlerman, E. J., K. K. Droegemeier, and R. Davies-Jones, 1999: A Numerical Simulation of Cyclic Mesocyclogenesis. *J. Atmos. Sci.*, **56 (13)**, 2045–2069, https://doi.org/10.1175/1520-0469(1999)056⟨2045:ANSOCM⟩2.0.CO;2, URL https://doi.org/10.1175/1520-0469(1999)056⟨2045:ANSOCM⟩2.0.CO;2, https://journals.ametsoc.org/jas/article-pdf/56/13/2045/3440866/1520-0469(1999)056_2045_ansocm_2_0_co_2.pdf.

Anderson-Frey, A. K., Y. P. Richardson, A. R. Dean, R. L. Thompson, and B. T. Smith, 2016: Investigation of Near-Storm Environments for Tornado Events and Warnings. *Wea. Forecasting*, **31 (6)**, 1771–1790, https://doi.org/10.1175/WAF-D-16-0046.1, URL https://doi.org/10.1175/WAF-D-16-0046.1, https://journals.ametsoc.org/waf/article-pdf/31/6/1771/4661190/waf-d-16-0046_1.pdf.

Anderson-Frey, A. K., Y. P. Richardson, A. R. Dean, R. L. Thompson, and B. T. Smith, 2017: Self-Organizing Maps for the Investigation of Tornadic Near-Storm Environments. *Wea. Forecasting*, **32 (4)**, 1467–1475, https://doi.org/10.1175/WAF-D-17-0034.1, URL https://doi.org/10.1175/WAF-D-17-0034.1, https://journals.ametsoc.org/waf/article-pdf/32/4/1467/4667773/waf-d-17-0034_1.pdf.

Benjamin, S. G., and Coauthors, 2004: An Hourly Assimilation–Forecast Cycle: The RUC. *Mon. Wea. Rev.*, **132 (2)**, 495–518, https://doi.org/10.1175/1520-0493(2004)132⟨0495:AHACTR⟩2.0.CO;2, URL https://doi.org/10.1175/1520-0493(2004)132⟨0495:AHACTR⟩2.0.CO;2, https://journals.ametsoc.org/mwr/article-pdf/132/2/495/4210534/1520-0493(2004)132_0495_ahactr_2_0_co_2.pdf.

Benjamin, S. G., and Coauthors, 2016: A North American Hourly Assimilation and Model Forecast Cycle: The Rapid Refresh. *Mon. Wea. Rev.*, **144 (4)**, 1669–1694, https://doi.org/10.1175/MWR-D-15-0242.1, URL https://doi.org/10.1175/MWR-D-15-0242.1, https://journals.ametsoc.org/mwr/article-pdf/144/4/1669/4334616/mwr-d-15-0242_1.pdf.

Blanchard, D. O., and J. M. Straka, 1998: Some possible mechanisms for tornadogenesis failure in a supercell. *Preprints, 19th Conf. on Severe Local Storms, Minneapolis, MN*, Amer. Meteor. Soc., 116–119.

Accepted for publication in *Journal of the Atmospheric Sciences*. DOI 10.1175/JAS-D-22-0253.1.

Bothwell, P. J., J. Hart, and R. L. Thompson, 2002: An integrated three-dimensional objective analysis scheme in use at the Storm Prediction Center. *21st Conf. on Severe Local Storms, San Antonio, TX*, Amer. Meteor. Soc., jP3.1.

Brooks, H. E., J. W. Lee, and J. P. Craven, 2003: The spatial distribution of severe thunderstorm and tornado environments from global reanalysis data. *Atmospheric Research*, **67-68**, 73–94, https://doi.org/https://doi.org/10.1016/S0169-8095(03)00045-0, URL https://www.sciencedirect.com/science/article/pii/S0169809503000450, european Conference on Severe Storms 2002.

Brotzge, J., S. Erickson, and H. Brooks, 2011: A 5-yr Climatology of Tornado False Alarms. *Wea. Forecasting*, **26 (4)**, 534–544, https://doi.org/10.1175/WAF-D-10-05004.1, URL https://doi.org/10.1175/WAF-D-10-05004.1, https://journals.ametsoc.org/waf/article-pdf/26/4/534/4647257/waf-d-10-05004_1.pdf.

Bryan, G. H., and J. M. Fritsch, 2002: A Benchmark Simulation for Moist Nonhydrostatic Numerical Models. *Mon. Wea. Rev.*, **130 (12)**, 2917–2928, https://doi.org/10.1175/1520-0493(2002)130⟨2917:ABSFMN⟩2.0.CO;2, URL https://doi.org/10.1175/1520-0493(2002)130⟨2917:ABSFMN⟩2.0.CO;2, https://journals.ametsoc.org/mwr/article-pdf/130/12/2917/4198716/1520-0493(2002)130_2917_absfmn_2_0_co_2.pdf.

Bunkers, M. J., 2018: Observations of Right-Moving Supercell Motion Forecast Errors. *Wea. Forecasting*, **33 (1)**, 145–159, https://doi.org/10.1175/WAF-D-17-0133.1, URL https://doi.org/10.1175/WAF-D-17-0133.1, https://journals.ametsoc.org/waf/article-pdf/33/1/145/4671175/waf-d-17-0133_1.pdf.

Bunkers, M. J., J. S. Johnson, L. J. Czepyha, J. M. Grzywacz, B. A. Klimowski, and M. R. Hjelmfelt, 2006: An Observational Examination of Long-Lived Supercells. Part II: Environmental Conditions and Forecasting. *Wea. Forecasting*, **21 (5)**, 689–714, https://doi.org/10.1175/WAF952.1, URL https://doi.org/10.1175/WAF952.1, https://journals.ametsoc.org/waf/article-pdf/21/5/689/4639415/waf952_1.pdf.

Bunkers, M. J., B. A. Klimowski, J. W. Zeitler, R. L. Thompson, and M. L. Weisman, 2000: Predicting Supercell Motion Using a New Hodograph Technique. *Wea. Forecasting*, **15 (1)**,

Accepted for publication in *Journal of the Atmospheric Sciences*. DOI 10.1175/JAS-D-22-0253.1.

61–79, https://doi.org/10.1175/1520-0434(2000)015⟨0061:PSMUAN⟩2.0.CO;2, URL https://doi.org/10.1175/1520-0434(2000)015⟨0061:PSMUAN⟩2.0.CO;2, https://journals.ametsoc.org/waf/article-pdf/15/1/61/4629676/1520-0434(2000)015_0061_psmuan_2_0_co_2.pdf.

Clark, M. R., D. J. Parker, and K. E. Hanley, 2021: synoptic-scale and mesoscale controls for tornadogenesis on cold fronts: Shear-zone vortex-genesis in a developing frontal wave. *Quart. J. Roy. Meteor. Soc.*, **147**, 3979–4009, https://doi.org/10.1002/qj.4164, URL https://rmets.onlinelibrary.wiley.com/doi/pdf/10.1002/qj.4164.

Coffer, B. E., and M. D. Parker, 2015: Impacts of Increasing Low-Level Shear on Supercells during the Early Evening Transition. *Mon. Wea. Rev.*, **143 (5)**, 1945–1969, https://doi.org/10.1175/MWR-D-14-00328.1, URL https://doi.org/10.1175/MWR-D-14-00328.1, https://journals.ametsoc.org/mwr/article-pdf/143/5/1945/4318622/mwr-d-14-00328_1.pdf.

Coffer, B. E., and M. D. Parker, 2017: Simulated Supercells in Nontornadic and Tornadic VORTEX2 Environments. *Mon. Wea. Rev.*, **145 (1)**, 149–180, https://doi.org/10.1175/MWR-D-16-0226.1, URL https://doi.org/10.1175/MWR-D-16-0226.1, https://journals.ametsoc.org/mwr/article-pdf/145/1/149/4361091/mwr-d-16-0226_1.pdf.

Coffer, B. E., and M. D. Parker, 2018: Is There a "Tipping Point" between Simulated Nontornadic and Tornadic Supercells in VORTEX2 Environments? *Mon. Wea. Rev.*, **146 (8)**, 2667–2693, https://doi.org/10.1175/MWR-D-18-0050.1, URL https://doi.org/10.1175/MWR-D-18-0050.1, https://journals.ametsoc.org/mwr/article-pdf/146/8/2667/4386012/mwr-d-18-0050_1.pdf.

Coffer, B. E., M. D. Parker, J. M. L. Dahl, L. J. Wicker, and A. J. Clark, 2017: Volatility of Tornadogenesis: An Ensemble of Simulated Nontornadic and Tornadic Supercells in VORTEX2 Environments. *Mon. Wea. Rev.*, **145 (11)**, 4605–4625, https://doi.org/10.1175/MWR-D-17-0152.1, URL https://doi.org/10.1175/MWR-D-17-0152.1, https://journals.ametsoc.org/mwr/article-pdf/145/11/4605/4361600/mwr-d-17-0152_1.pdf.

Coffer, B. E., M. D. Parker, J. M. Peters, and A. R. Wade, 2022: Supercell low-level mesocyclones: Origins of inflow and vorticity. *Mon. Wea. Rev.*, URL https://doi.org/10.48550/arXiv.2210.03715.

Accepted for publication in *Journal of the Atmospheric Sciences*. DOI 10.1175/JAS-D-22-0253.1.

Coffer, B. E., M. D. Parker, R. L. Thompson, B. T. Smith, and R. E. Jewell, 2019: Using Near-Ground Storm Relative Helicity in Supercell Tornado Forecasting. *Wea. Forecasting*, **34 (5)**, 1417–1435, https://doi.org/10.1175/WAF-D-19-0115.1, URL https://doi.org/10.1175/WAF-D-19-0115.1, https://journals.ametsoc.org/waf/article-pdf/34/5/1417/4883068/waf-d-19-0115_1.pdf.

Coffer, B. E., M. Taszarek, and M. D. Parker, 2020: Near-ground wind profiles of tornadic and nontornadic environments in the united states and europe from era5 reanalyses. *Weather and Forecasting*, **35 (6)**, 2621 – 2638, https://doi.org/10.1175/WAF-D-20-0153.1, URL https://journals.ametsoc.org/view/journals/wefo/35/6/waf-d-20-0153.1.xml.

Coniglio, M. C., and M. D. Parker, 2020: Insights into supercells and their environments from three decades of targeted radiosonde observations. *Monthly Weather Review*, **148 (12)**, 4893 – 4915, https://doi.org/10.1175/MWR-D-20-0105.1, URL https://journals.ametsoc.org/view/journals/mwre/148/12/mwr-d-20-0105.1.xml.

Dahl, J. M. L., 2015: Near-Ground Rotation in Simulated Supercells: On the Robustness of the Baroclinic Mechanism. *Mon. Wea. Rev.*, **143 (12)**, 4929–4942, https://doi.org/10.1175/MWR-D-15-0115.1, URL https://doi.org/10.1175/MWR-D-15-0115.1, https://journals.ametsoc.org/mwr/article-pdf/143/12/4929/4305849/mwr-d-15-0115_1.pdf.

Davies-Jones, R., 1984: Streamwise Vorticity: The Origin of Updraft Rotation in Supercell Storms. *J. Atmos. Sci.*, **41 (20)**, 2991–3006, https://doi.org/10.1175/1520-0469(1984)041⟨2991:SVTOOU⟩2.0.CO;2, URL https://doi.org/10.1175/1520-0469(1984)041⟨2991:SVTOOU⟩2.0.CO;2, https://journals.ametsoc.org/jas/article-pdf/41/20/2991/3422612/1520-0469(1984)041_2991_svtoou_2_0_co_2.pdf.

Davies-Jones, R., 2015: A review of supercell and tornado dynamics. *Atmos. Res.*, **158**, 274–291, https://doi.org/10.1016/j.atmosres.2014.04.007.

Davies-Jones, R., and H. Brooks, 1993: *The Tornado: Its Structure, Dynamics, Prediction, and Hazards*, chap. Mesocyclogenesis from a theoretical perspective, 105–114. Geophysical Monograph Series, Amer. Geophys. Union.

Davies-Jones, R., R. J. Trapp, and H. Brooks., 2001: *Severe Convective Storms*, 167–221. Springer.

Accepted for publication in *Journal of the Atmospheric Sciences*. DOI 10.1175/JAS-D-22-0253.1.

Davies-Jones, R. P., D. W. Burgess, and M. Foster, 1990: Test of helicity as a tornado forecast parameter. *Preprints, 16th Conf. on Severe Local Storms, Kananaskis Park, AB, Canada*, Amer. Meteor. Soc., 588–592.

Esterheld, J. M., and D. J. Giuliano, 2008: Discriminating between tornadic and non-tornadic supercells: A new hodograph technique. *Electron. J. Severe Storms Meteor.*, **3 (2)**.

Fischer, J., and J. M. L. Dahl, 2020: The Relative Importance of Updraft and Cold Pool Characteristics on Supercell Tornadogenesis in Highly Idealized Simulations. *J. Atmos. Sci.*, 1–53, https://doi.org/10.1175/JAS-D-20-0126.1, URL https://doi.org/10.1175/JAS-D-20-0126.1, https://journals.ametsoc.org/jas/article-pdf/doi/10.1175/JAS-D-20-0126.1/5003819/jasd200126.pdf.

Flournoy, M. D., M. C. Coniglio, E. N. Rasmussen, J. C. Furtado, and B. E. Coffer, 2020: Modes of Storm-Scale Variability and Tornado Potential in VORTEX2 Near- and Far-Field Tornadic Environments. *Mon. Wea. Rev.*, **148 (10)**, 4185 – 4207, https://doi.org/10.1175/MWR-D-20-0147.1, URL https://journals.ametsoc.org/view/journals/mwre/148/10/mwrD200147.xml.

Goldacker, N. A., and M. D. Parker, 2021: Low-level updraft intensification in response to environmental wind profiles. *Journal of the Atmospheric Sciences*, **78 (9)**, 2763 – 2781, https://doi.org/10.1175/JAS-D-20-0354.1, URL https://journals.ametsoc.org/view/journals/atsc/78/9/JAS-D-20-0354.1.xml.

Grzych, M. L., B. D. Lee, and C. A. Finley, 2007: Thermodynamic analysis of supercell rear-flank downdrafts from project answers. *Mon. Wea. Rev.*, **135**, 240–246.

Klees, A. M., Y. P. Richardson, P. M. Markowski, C. Weiss, J. M. Wurman, and K. K. Kosiba, 2016: Comparison of the Tornadic and Nontornadic Supercells Intercepted by VORTEX2 on 10 June 2010. *Mon. Wea. Rev.*, **144 (9)**, 3201–3231, https://doi.org/10.1175/MWR-D-15-0345.1, URL https://doi.org/10.1175/MWR-D-15-0345.1, https://journals.ametsoc.org/mwr/article-pdf/144/9/3201/4356112/mwr-d-15-0345_1.pdf.

Kohonen, T., 1982: Self-organized formation of topologically correct feature maps. *Biol. Cybern.*, **43 (1)**, 59–69, https://doi.org/10.1007/BF00337288, URL https://doi.org/10.1007/BF00337288.

Kohonen, T., 1990: The self-organizing map. *Proceedings of the IEEE*, **78 (9)**, 1464–1480.

Accepted for publication in *Journal of the Atmospheric Sciences*. DOI 10.1175/JAS-D-22-0253.1.

Kohonen, T., 1997: *Self-Organizing Maps 2nd edition*. Springer Series in Information Sciences, Springer-Verlag Berlin Heidelberg, 426 pp.

Mansell, E. R., C. L. Ziegler, and E. C. Bruning, 2010: Simulated electrification of a small thunderstorm with two-moment bulk microphysics. *Journal of the Atmospheric Sciences*, **67 (1)**, 171 – 194, https://doi.org/10.1175/2009JAS2965.1, URL https://journals.ametsoc.org/view/journals/atsc/67/1/2009jas2965.1.xml.

Markowski, P., C. Hannon, J. Frame, E. Lancaster, A. Pietrycha, R. Edwards, and R. L. Thompson, 2003: Characteristics of Vertical Wind Profiles near Supercells Obtained from the Rapid Update Cycle. *Wea. Forecasting*, **18 (6)**, 1262–1272, https://doi.org/10.1175/1520-0434(2003)018⟨1262:COVWPN⟩2.0.CO;2, URL https://doi.org/10.1175/1520-0434(2003)018⟨1262:COVWPN⟩2.0.CO;2, https://journals.ametsoc.org/waf/article-pdf/18/6/1262/4634685/1520-0434(2003)018_1262_covwpn_2_0_co_2.pdf.

Markowski, P., Y. Richardson, E. Rasmussen, J. Straka, R. Davies-Jones, and R. J. Trapp, 2008: Vortex Lines within Low-Level Mesocyclones Obtained from Pseudo-Dual-Doppler Radar Observations. *Mon. Wea. Rev.*, **136 (9)**, 3513–3535, https://doi.org/10.1175/2008MWR2315.1, URL https://doi.org/10.1175/2008MWR2315.1, https://journals.ametsoc.org/mwr/article-pdf/136/9/3513/4242494/2008mwr2315_1.pdf.

Markowski, P., and Coauthors, 2012: The Pretornadic Phase of the Goshen County, Wyoming, Supercell of 5 June 2009 Intercepted by VORTEX2. Part II: Intensification of Low-Level Rotation. *Mon. Wea. Rev.*, **140 (9)**, 2916–2938, https://doi.org/10.1175/MWR-D-11-00337.1, URL https://doi.org/10.1175/MWR-D-11-00337.1, https://journals.ametsoc.org/mwr/article-pdf/140/9/2916/4275239/mwr-d-11-00337_1.pdf.

Markowski, P. M., 2016: An Idealized Numerical Simulation Investigation of the Effects of Surface Drag on the Development of Near-Surface Vertical Vorticity in Supercell Thunderstorms. *J. Atmos. Sci.*, **73 (11)**, 4349–4385, https://doi.org/10.1175/JAS-D-16-0150.1, URL https://doi.org/10.1175/JAS-D-16-0150.1, https://journals.ametsoc.org/jas/article-pdf/73/11/4349/3863768/jas-d-16-0150_1.pdf.

Accepted for publication in *Journal of the Atmospheric Sciences*. DOI 10.1175/JAS-D-22-0253.1.

Markowski, P. M., Y. Richardson, M. Majcen, J. Marquis, and J. Wurman, 2011: Characteristics of the wind field in three nontornadic low-level mesocyclones observed by the Doppler on Wheels radars. *Electron. J. Severe Storms Meteor.*, **6 (3)**.

Markowski, P. M., and Y. P. Richardson, 2014: The Influence of Environmental Low-Level Shear and Cold Pools on Tornadogenesis: Insights from Idealized Simulations. *J. Atmos. Sci.*, **71 (1)**, 243–275, https://doi.org/10.1175/JAS-D-13-0159.1, URL https://doi.org/10.1175/JAS-D-13-0159.1, https://journals.ametsoc.org/jas/article-pdf/71/1/243/3643392/jas-d-13-0159_1.pdf.

Markowski, P. M., J. M. Straka, and E. N. Rasmussen, 2002: Direct Surface Thermodynamic Observations within the Rear-Flank Downdrafts of Nontornadic and Tornadic Supercells. *Mon. Wea. Rev.*, **130 (7)**, 1692–1721, https://doi.org/10.1175/1520-0493(2002)130⟨1692:DSTOWT⟩2.0.CO;2, URL https://doi.org/10.1175/1520-0493(2002)130⟨1692:DSTOWT⟩2.0.CO;2, https://journals.ametsoc.org/mwr/article-pdf/130/7/1692/4208125/1520-0493(2002)130_1692_dstowt_2_0_co_2.pdf.

Naylor, J., and M. S. Gilmore, 2012: Convective initiation in an idealized cloud model using an updraft nudging technique. *Monthly Weather Review*, **140 (11)**, 3699 – 3705, https://doi.org/10.1175/MWR-D-12-00163.1, URL https://journals.ametsoc.org/view/journals/mwre/140/11/mwr-d-12-00163.1.xml.

Nowotarski, C. J., and A. A. Jensen, 2013: Classifying Proximity Soundings with Self-Organizing Maps toward Improving Supercell and Tornado Forecasting. *Wea. Forecasting*, **28 (3)**, 783–801, https://doi.org/10.1175/WAF-D-12-00125.1, URL https://doi.org/10.1175/WAF-D-12-00125.1, https://journals.ametsoc.org/waf/article-pdf/28/3/783/4655143/waf-d-12-00125_1.pdf.

Nowotarski, C. J., and E. A. Jones, 2018: Multivariate Self-Organizing Map Approach to Classifying Supercell Tornado Environments Using Near-Storm, Low-Level Wind and Thermodynamic Profiles. *Wea. Forecasting*, **33 (3)**, 661–670, https://doi.org/10.1175/WAF-D-17-0189.1, URL https://doi.org/10.1175/WAF-D-17-0189.1, https://journals.ametsoc.org/waf/article-pdf/33/3/661/4664844/waf-d-17-0189_1.pdf.

Orf, L., R. Wilhelmson, B. Lee, C. Finley, and A. Houston, 2017: Evolution of a Long-Track Violent Tornado within a Simulated Supercell. *Bull. Amer. Meteor. Soc.*, **98 (1)**, 45

Accepted for publication in *Journal of the Atmospheric Sciences*. DOI 10.1175/JAS-D-22-0253.1.

– 68, https://doi.org/10.1175/BAMS-D-15-00073.1, URL https://journals.ametsoc.org/view/journals/bams/98/1/bams-d-15-00073.1.xml.

Parker, M. D., 2014: Composite VORTEX2 Supercell Environments from Near-Storm Soundings. *Mon. Wea. Rev.*, **142 (2)**, 508–529, https://doi.org/10.1175/MWR-D-13-00167.1, URL https://doi.org/10.1175/MWR-D-13-00167.1, https://journals.ametsoc.org/mwr/article-pdf/142/2/508/4297856/mwr-d-13-00167_1.pdf.

Parker, M. D., and J. M. L. Dahl, 2015: Production of Near-Surface Vertical Vorticity by Idealized Downdrafts. *Mon. Wea. Rev.*, **143 (7)**, 2795–2816, https://doi.org/10.1175/MWR-D-14-00310.1, URL https://doi.org/10.1175/MWR-D-14-00310.1, https://journals.ametsoc.org/mwr/article-pdf/143/7/2795/4345586/mwr-d-14-00310_1.pdf.

Peters, J. M., B. E. Coffer, M. D. Parker, C. J. Nowotarski, J. P. Mulholland, C. J. Nixon, and J. T. Allen, 2022: Disentangling the influences of storm-relative flow and horizontal streamwise vorticity on low-level mesocyclones in supercells. *Journal of the Atmospheric Sciences*, https://doi.org/10.1175/JAS-D-22-0114.1, URL https://journals.ametsoc.org/view/journals/atsc/aop/JAS-D-22-0114.1/JAS-D-22-0114.1.xml.

Peters, J. M., C. J. Nowotarski, J. P. Mulholland, and R. L. Thompson, 2020: The influences of effective inflow layer streamwise vorticity and storm-relative flow on supercell updraft properties. *Journal of the Atmospheric Sciences*, **77 (9)**, 3033 – 3057, https://doi.org/10.1175/JAS-D-19-0355.1, URL https://journals.ametsoc.org/view/journals/atsc/77/9/jasD190355.xml.

Rasmussen, E. N., and D. O. Blanchard, 1998: A Baseline Climatology of Sounding-Derived Supercell andTornado Forecast Parameters. *Wea. Forecasting*, **13 (4)**, 1148–1164, https://doi.org/10.1175/1520-0434(1998)013⟨1148:ABCOSD⟩2.0.CO;2, URL https://doi.org/10.1175/1520-0434(1998)013⟨1148:ABCOSD⟩2.0.CO;2, https://journals.ametsoc.org/waf/article-pdf/13/4/1148/4627972/1520-0434(1998)013_1148_abcosd_2_0_co_2.pdf.

Roberts, B., and M. Xue, 2017: The Role of Surface Drag in Mesocyclone Intensification Leading to Tornadogenesis within an Idealized Supercell Simulation. *J. Atmos. Sci.*, **74**, 3055–3077, https://doi.org/10.1175/JAS-D-16-0364.1.

Accepted for publication in *Journal of the Atmospheric Sciences*. DOI 10.1175/JAS-D-22-0253.1.

Roberts, B., M. Xue, and I. Dawson, Daniel T., 2020: The Effect of Surface Drag Strength on Mesocyclone Intensification and Tornadogenesis in Idealized Supercell Simulations. *J. Atmos. Sci.*, **77**, 1699–1721, https://doi.org/10.1175/JAS-D-19-0109.1.

Roberts, B., M. Xue, A. D. Schenkman, and I. Dawson, Daniel T., 2016: The Role of Surface Drag in Tornadogenesis within an Idealized Supercell Simulation. *J. Atmos. Sci.*, **73 (9)**, 3371–3395, https://doi.org/10.1175/JAS-D-15-0332.1, URL https://doi.org/10.1175/JAS-D-15-0332.1, https://journals.ametsoc.org/jas/article-pdf/73/9/3371/3859791/jas-d-15-0332_1.pdf.

Rotunno, R., and J. Klemp, 1985: On the Rotation and Propagation of Simulated Supercell Thunderstorms. *J. Atmos. Sci.*, **42 (3)**, 271–292, https://doi.org/10.1175/1520-0469(1985)042⟨0271:OTRAPO⟩2.0.CO;2, URL https://doi.org/10.1175/1520-0469(1985)042⟨0271:OTRAPO⟩2.0.CO;2, https://journals.ametsoc.org/jas/article-pdf/42/3/271/3423160/1520-0469(1985)042_0271_otrapo_2_0_co_2.pdf.

Schenkman, A. D., M. Xue, and M. Hu, 2014: Tornadogenesis in a High-Resolution Simulation of the 8 May 2003 Oklahoma City Supercell. *J. Atmos. Sci.*, **71 (1)**, 130–154, https://doi.org/10.1175/JAS-D-13-073.1, URL https://doi.org/10.1175/JAS-D-13-073.1, https://journals.ametsoc.org/jas/article-pdf/71/1/130/3642761/jas-d-13-073_1.pdf.

Skinner, P. S., C. C. Weiss, M. M. French, H. B. Bluestein, P. M. Markowski, and Y. P. Richardson, 2014: VORTEX2 Observations of a Low-Level Mesocyclone with Multiple Internal Rear-Flank Downdraft Momentum Surges in the 18 May 2010 Dumas, Texas, Supercell. *Mon. Wea. Rev.*, **142 (8)**, 2935–2960, https://doi.org/10.1175/MWR-D-13-00240.1, URL https://doi.org/10.1175/MWR-D-13-00240.1, https://journals.ametsoc.org/mwr/article-pdf/142/8/2935/4313810/mwr-d-13-00240_1.pdf.

Smith, B. T., R. L. Thompson, J. S. Grams, C. Broyles, and H. E. Brooks, 2012: Convective Modes for Significant Severe Thunderstorms in the Contiguous United States. Part I: Storm Classification and Climatology. *Wea. Forecasting*, **27 (5)**, 1114–1135, https://doi.org/10.1175/WAF-D-11-00115.1, URL https://doi.org/10.1175/WAF-D-11-00115.1, https://journals.ametsoc.org/waf/article-pdf/27/5/1114/4652258/waf-d-11-00115_1.pdf.

Thompson, R. L., R. Edwards, J. A. Hart, K. L. Elmore, and P. Markowski, 2003: Close Proximity Soundings within Supercell Environments Obtained from the Rapid Update Cy-

Accepted for publication in *Journal of the Atmospheric Sciences*. DOI 10.1175/JAS-D-22-0253.1.

cle. *Wea. Forecasting*, **18 (6)**, 1243–1261, https://doi.org/10.1175/1520-0434(2003)018⟨1243:CPSWSE⟩2.0.CO;2, URL https://doi.org/10.1175/1520-0434(2003)018⟨1243:CPSWSE⟩2.0.CO;2, https://journals.ametsoc.org/waf/article-pdf/18/6/1243/4637557/1520-0434(2003)018_1243_cpswse_2_0_co_2.pdf.

Thompson, R. L., C. M. Mead, and R. Edwards, 2007: Effective Storm-Relative Helicity and Bulk Shear in Supercell Thunderstorm Environments. *Wea. Forecasting*, **22 (1)**, 102–115, https://doi.org/10.1175/WAF969.1, URL https://doi.org/10.1175/WAF969.1, https://journals.ametsoc.org/waf/article-pdf/22/1/102/4638808/waf969_1.pdf.

Thompson, R. L., B. T. Smith, J. S. Grams, A. R. Dean, and C. Broyles, 2012: Convective Modes for Significant Severe Thunderstorms in the Contiguous United States. Part II: Supercell and QLCS Tornado Environments. *Wea. Forecasting*, **27 (5)**, 1136–1154, https://doi.org/10.1175/WAF-D-11-00116.1, URL https://doi.org/10.1175/WAF-D-11-00116.1, https://journals.ametsoc.org/waf/article-pdf/27/5/1136/4651150/waf-d-11-00116_1.pdf.

Trapp, R. J., 1999: Observations of Nontornadic Low-Level Mesocyclones and Attendant Tornadogenesis Failure during VORTEX. *Mon. Wea. Rev.*, **127 (7)**, 1693–1705, https://doi.org/10.1175/1520-0493(1999)127⟨1693:OONLLM⟩2.0.CO;2, URL https://doi.org/10.1175/1520-0493(1999)127⟨1693:OONLLM⟩2.0.CO;2, https://journals.ametsoc.org/mwr/article-pdf/127/7/1693/4186653/1520-0493(1999)127_1693_oonllm_2_0_co_2.pdf.

Vettigli, G., 2019: MiniSom: Minimalistic and NumPy-based implementation of the Self Organizing Map. Version 2.2.3, https://github.com/JustGlowing/minisom.

Wakimoto, R. M., and H. Cai, 2000: Analysis of a Nontornadic Storm during VORTEX 95. *Mon. Wea. Rev.*, **128 (3)**, 565–592, https://doi.org/10.1175/1520-0493(2000)128⟨0565:AOANSD⟩2.0.CO;2, URL https://doi.org/10.1175/1520-0493(2000)128⟨0565:AOANSD⟩2.0.CO;2, https://journals.ametsoc.org/mwr/article-pdf/128/3/565/4190730/1520-0493(2000)128_0565_aoansd_2_0_co_2.pdf.

Warren, R. A., H. Richter, and R. L. Thompson, 2021: Spectrum of near-storm environments for significant severe right-moving supercells in the contiguous United States. *Monthly Weather Review*, **149 (10)**, 3299 – 3323, https://doi.org/10.1175/MWR-D-21-0006.1, URL https://journals.ametsoc.org/view/journals/mwre/149/10/MWR-D-21-0006.1.xml.

Accepted for publication in *Journal of the Atmospheric Sciences*. DOI 10.1175/JAS-D-22-0253.1.

Wicker, L. J., and R. B. Wilhelmson, 1995: Simulation and Analysis of Tornado Development and Decay within a Three-Dimensional Supercell Thunderstorm. *J. Atmos. Sci.*, **52 (15)**, 2675–2703, https://doi.org/10.1175/1520-0469(1995)052⟨2675:SAAOTD⟩2.0.CO;2, URL https://doi.org/10.1175/1520-0469(1995)052⟨2675:SAAOTD⟩2.0.CO;2, https://journals.ametsoc.org/jas/article-pdf/52/15/2675/3918434/1520-0469(1995)052_2675_saaotd_2_0_co_2.pdf.

Yokota, S., H. Niino, H. Seko, M. Kunii, and H. Yamauchi, 2018: Important Factors for Tornadogenesis as Revealed by High-Resolution Ensemble Forecasts of the Tsukuba Supercell Tornado of 6 May 2012 in Japan. *Mon. Wea. Rev.*, **146 (4)**, 1109 – 1132, https://doi.org/10.1175/MWR-D-17-0254.1, URL https://journals.ametsoc.org/view/journals/mwre/146/4/mwr-d-17-0254.1.xml.

Zeitler, J. W., and M. J. Bunkers, 2005: Operational forecasting of supercell motion: Review and case studies using multiple datasets. *Natl. Weather Dig.*, **29**, 81–97.

Accepted for publication in *Journal of the Atmospheric Sciences*. DOI 10.1175/JAS-D-22-0253.1.